Aerosol radiative effects in the ultraviolet, visible, and near-infrared spectral ranges using long-term aerosol data series over the Iberian Peninsula

D. Mateos[1,2], M. Antón[1], C. Toledano[2], V. E. Cachorro[2], L. Alados-Arboledas[3,4], M. Sorribas[3,4,5], M.J. Costa[6], J.M. Baldasano[7].

1. Departamento de Física, Universidad de Extremadura, Badajoz, Spain

2. Grupo de Óptica Atmosférica, Universidad de Valladolid, Valladolid, Spain

3. Departamento de Física Aplicada, Universidad de Granada, Granada, Spain

4. Andalusian Institute for Earth System Research, Universidad de Granada, Granada, Spain

5. Estación de Sondeos Atmosféricos El Arenosillo, INTA, Huelva, Spain

6. Évora Geophysics Centre and Dep. Physics, University of Évora, Évora, Portugal

7. Universidad Politécnica de Cataluña, Barcelona, Spain

Corresponding author: D. Mateos, Grupo de Óptica Atmosférica, Universidad de Valladolid, Paseo Belén 7, 47011, Valladolid, Spain. E-mail: mateos@goa.uva.es

Abstract

A better understanding of the aerosol radiative properties is a crucial challenge for climate change studies. This study aims to provide a complete characterization of aerosol radiative effects in different spectral ranges within the shortwave (SW) solar spectrum. For this purpose, long-term datasets of aerosol properties from six AERONET stations located in the Iberian Peninsula (Southwestern Europe) are analyzed in term of climatological characterization and trends. Aerosol information is used as input to the libRadtran model in order to determine the aerosol radiative effect at the surface in the ultraviolet (ARE_{UV}), visible (ARE_{VIS}), near-infrared (ARE_{NIR}), and the entire SW range (ARE_{SW}) under cloud-free conditions. Over the whole Iberian Peninsula, yearly aerosol radiative effects in the different spectral ranges are: $-1.1 < ARE_{UV} < -0.7$ W m^{-2}, $-5.7 < ARE_{VIS} < -3.5$ W m^{-2}, $-2.6 < ARE_{NIR} < -1.6$ W m^{-2}, and $-8.8 < ARE_{SW} < -5.7$ W m^{-2}. The four variables showed positive statistically significant trends between 2004 and 2012, e.g., ARE_{SW} increased +3.6 W m^{-2} per decade. This fact is linked to the decrease in the aerosol load, which presents a trend of -0.04 unit of aerosol optical depth at 500 nm per decade, hence a reduction of aerosol effect on solar radiation at the surface is seen. Monthly means of ARE show a seasonal pattern with larger values in spring and summer. The aerosol forcing efficiency (AFE), ARE per unit of aerosol optical depth, is also evaluated in the four spectral ranges. AFE exhibits a dependence on single scattering albedo and a weaker one on Ångström exponent. AFE is larger (in absolute value) for small and absorbing particles. The contributions of the UV, VIS, and NIR ranges to the SW efficiency vary with the aerosol types. Aerosol size determines the fractions of AFE_{VIS}/AFE_{SW} and AFE_{NIR}/AFE_{SW}. VIS range is the dominant region for all types, although non-absorbing large particles cause a more equal contribution of VIS and NIR intervals. The AFE_{UV}/AFE_{SW} ratio shows a higher contribution for absorbing fine particles.

1. Introduction

Atmospheric aerosol particles can absorb and scatter part of the total amount of solar radiation entering the Earth's atmosphere. In fact, aerosols directly influence the Earth's energy budget and act as cloud condensation nuclei modifying the cloud structure (e.g., Boucher et al., 2013). Aerosols can either be produced by ejection into the atmosphere or by physical and chemical processes within the atmosphere. Aerosol particles affect the radiative field by attenuating the direct component thereby enhancing (or reducing under a highly absorbing aerosol) the diffuse one. They also produce indirect effects by perturbing the Earth's atmospheric radiative balance by modulating cloud albedo and fraction.

The aerosol radiative effect (ARE) is defined as the change in net radiation due to changes in atmospheric aerosol properties and content. This is a key quantity in the determination of climate change (e.g., Hansen et al., 1998). Most studies dealing with ARE have focused on discrete wavelengths, whole shortwave (SW) solar radiation spectrum (e.g., Rajeev and Ramanathan, 2001; García et al., 2008; di Sarra et al., 2008; Foyo-Moreno et al., 2014; Mateos et al., 2013a), longwave (LW) radiation (e.g., Panicker et al., 2008; di Sarra et al., 2011; Antón et al., 2014), ultraviolet (UV) interval (e.g., Hatzianastassiou et al., 2004; Kazadzis et al., 2009; Nikitidou et al., 2013), and visible (VIS) range (e.g., Jayaraman et al., 1998; Horvath et al., 2002; Bush and Valero, 2003; Meloni et al., 2003). With regards to surface SW radiative effect (ARE_{SW}), Di Biagio et al. (2010) obtained the maximum radiative daily effects for different aerosol types in the central Mediterranean in the period 2004-2007: -61 Wm^{-2} (desert dust aerosols), -26 Wm^{-2} (urban/industrial - biomass burning aerosols) and -43 Wm^{-2} (mixed aerosols). All these negative figures point out a cooling of the Earth's surface. Aerosol radiative effects for dust particles, for which the LW effect is relevant, in the LW (ARE_{LW}) are expected to be smaller than in the SW and with positive sign (see, e.g., di Sarra et al., 2011; Antón et al., 2014). Hence, this heating effect at the surface can partly offset the

68 cooling induced in the SW range. With respect to the ARE for the UV range (ARE_{UV}), Nikitidou et
69 al. (2013) analyzed the ARE in two different spectral regions in the UV range, 300-315 and 315-
70 360 nm. They found a stronger attenuation in the UV-B than in the UV-A.

71 The main goal of this study is to evaluate the ARE at the surface over the Iberian Peninsula, which
72 is a region of great interest because of its geographical position in Southwestern Europe, near the
73 African continent and the interface between the Atlantic Ocean and the Mediterranean Basin. Thus,
74 it is affected by frequent desert dust intrusions which modulate their aerosol climatology (Toledano
75 et al., 2007a, Bennouna et al., 2011; Pey et al., 2013; Valenzuela et al., 2012). In addition, this area
76 is also affected by a great variety of air masses loaded with different aerosol types: clean
77 continental, polluted plumes of central Europe, and marine aerosols. Hence, aerosol climatology at
78 six stations (Palencia, Barcelona, Cabo da Roca, Évora, Granada, and El Arenosillo) is also carried
79 out for different time periods between 2001 and 2012. Aerosol radiative effects as well as their
80 efficiency are calculated in four regions of the solar spectrum (ultraviolet, visible, near-infrared, and
81 shortwave) and the relative contribution of each range with respect to the whole solar spectrum is
82 analyzed as a function of the aerosol properties. Therefore, this study is intended to contribute to the
83 understanding of the aerosol impact on radiative budget over the Iberian Peninsula.

84 This article presents the following outline: detailed descriptions of the aerosol stations and the
85 database used are performed in Section 2; Section 3 includes the followed methodology; the results
86 obtained in the different analyses about the climatology of aerosol properties, aerosol radiative
87 effects, and aerosol forcing efficiencies are shown and discussed in Sections 4,5, and 6,
88 respectively. Finally, the main conclusions of this article are summarized in Section 7.

89

90

2. Columnar aerosol optical data

The aerosol data are obtained from the Aerosol Robotic Network (AERONET) (Holben et al., 1998). Six AERONET sites operating in the Iberian Peninsula are selected in this study: Palencia, Barcelona, Évora, Cabo da Roca, Granada and El Arenosillo (see Table 1), all of them with a minimum of 8 years of data sets of continuous observations. These sites present the largest records of aerosol properties in the Iberian Peninsula in the AERONET network.

The standard instrument used in AERONET is the Cimel CE-318 radiometer. It performs direct sun measurements at several wavelengths in the spectral range 340-1020 nm. Furthermore, the instrument also measures sky radiance in the solar almucantar and principal plane configurations at 440, 670, 870 and 1020 nm wavelengths. A detailed description of this instrument was provided by Holben et al. (1998). The direct sun observations are used to derive the spectral aerosol optical depth (AOD) and the corresponding Ångström exponent. The sky radiances together with the AOD are employed to retrieve a set of aerosol optical and microphysical properties via inversion methods (Dubovik and King, 2000; Dubovik et al., 2006). These include particle size distribution, complex refractive index, single scattering albedo (SSA), phase function, asymmetry parameter, fraction of non-spherical particles, etc. (see http://aeronet.gsfc.nasa.gov/new_web/Documents/Inversion_products_V2.pdf). Data are provided in three database levels: 1.0 (raw data), 1.5 (cloud-screened) and 2.0 (cloud-screened and quality assured).

The calibration of these instruments is performed following AERONET protocols by AERONET-NASA, PHOTONS and RIMA networks every 12 months of operation approximately. The estimated uncertainty is 0.01-0.02 for AOD (larger at shorter wavelengths) and ~5% for the sky radiances (Holben et al., 1998). The SSA has an absolute uncertainty about 0.03-0.07 depending on the aerosol load and type (Dubovik et al., 2000).

115 Level 2.0 aerosol optical depth data have been used in this work. However, it is well-known that
116 when level 2.0 inversion data are used, the number of available observations of single scattering
117 albedo (SSA) and asymmetry factor (g) is quite limited because these variables are only considered
118 reliable when $AOD_{440nm} > 0.4$[1]. Such AOD is mainly reached in the study region during Saharan
119 dust or biomass burning events, therefore we would not have information on SSA and g for other
120 conditions. To solve this issue, we have reduced the threshold of the level 2.0 inversion products.
121 For this, we started with the level 1.5 data (for those quality-assured almucantar data that reached
122 level 2.0) and applied the same criteria used by AERONET to elaborate the level 2.0 regarding the
123 number of symmetrical angles, retrieval error and solar zenith angle (see
124 http://aeronet.gsfc.nasa.gov/new_web/Documents/AERONETcriteria_final1_excerpt.pdf).
125 However, a less restrictive threshold is applied to the AOD, which we restricted to cases with
126 $AOD_{440nm} > 0.15$, instead of 0.4. This choice must be considered a compromise between the amount
127 and the quality of the data. This kind of approach has been adopted by other authors using
128 AERONET absorption data (e.g. Mallet et al., 2013). The threshold of 0.15 seems adequate
129 analyzing the typical values of the AOD in the Iberian Peninsula (e.g., Bennouna et al., 2011;
130 Obregón et al., 2012), because it can be considered a value to separate background aerosol
131 conditions from episodic events with moderate or high aerosol loadings. The level 1.5-filtered data
132 of SSA and g are daily averaged in order to have one value per day. In these conditions, the
133 estimated uncertainty of the single scattering albedo is ±0.05-0.07 (Dubovik et al., 2000).
134 Furthermore, for those days presenting level 2.0 data but also measurements in the 1.5-filtered level,
135 we tested the uncertainty of our approach. We evaluated the difference in the SSA values of the
136 level 1.5-filtered data with respect to the closest level 2.0 data. The mean relative differences in the

[1] Other inversion products, like the volume size distributions, are provided for all AOD levels.

SSA values between both methodologies are smaller than 1%, being in the same order that the inversion uncertainty.

Lastly, when the AOD is low (<0.15 at 440 nm), there is no reliable information on the absorption properties in the almucantar retrievals. Such low AOD is typical in our study region (e.g. almost 70% of observations at Palencia, Granada and Évora are below this threshold). If only cases with AOD_{440nm}>0.15 are considered in our study, the derived aerosol radiative effect would be unrealistically large. To overcome this problem of representativeness, fixed values of SSA (0.90) and g (0.75) have been used for the cases with AOD < 0.15 at 440 nm, considering typical values for continental, desert, and maritime aerosols (e.g., Hess et al., 1998). In spite of the associated uncertainties, our approximation (daily level 1.5-filtered values of these aerosol properties for AOD > 0.15 together with a typical fixed value for low AOD cases) provides a good characterization of the aerosol absorption of the particles present in the atmosphere. The data products and AERONET database level are summarized in Table 2, where the estimated absolute uncertainties of AOD and SSA are also provided.

3. Methodology

The ARE calculations are performed in the ultraviolet (ARE_{UV}, 280-400 nm), visible (ARE_{VIS}, 400-700 nm), near-infrared (ARE_{NIR}, 700-2800 nm), and shortwave (ARE_{SW}, 280-2800 nm) intervals. For this purpose, cloud-free simulations are carried out by means of a radiative transfer code.

The libRadtran model (Mayer and Kylling, 2005) has been shown to be a useful tool for obtaining solar radiation data, presenting high accuracy (e.g., Román et al., 2014). Version 1.7 of the libRadtran is used in this study with inputs of aerosol, total ozone column (TOC), precipitable water vapor column (PWC), and surface albedo data. We performed simulations of ultraviolet (280-400

nm), visible (400-700 nm), near-infrared (700-2800 nm), and shortwave (280-2800 nm) radiation during the periods indicated in Table 1. Total ozone column is provided by the Ozone Monitoring Instrument (OMI) and Total Ozone Mapping Spectrometer (TOMS). Daily values of these instruments are obtained from the Daily Level 3 Global Gridded products, which are downloaded using the Giovanni application (http://disc.sci.gsfc.nasa.gov/giovanni). Level 2.0 AERONET PWC data are used in the calculations. The uncertainty of this parameter is 10-15% (Holben et al., 1998). In addition, retrievals of surface albedo at 440, 675, 870 and 1020 nm from the AERONET algorithm are also used in this work. For land surface cover, this algorithm relies on the Lie–Ross model (Lucht and Roujean, 2000), but considering the bidirectional reflectance distributions from MODIS (Moody et al., 2005).

Aerosol properties obtained from AERONET measurements are also used as input to the libRadtran model. Ångström coefficients, α and β, are utilized to compute a spectral aerosol optical depth in the wavelengths of interest (Schuster et al., 2006). Ångström exponent α is obtained with the measurements between 440 and 870 nm, while the turbidity β is obtained from the α value and aerosol data at 1020 nm. Since the aerosol asymmetry factor, single scattering albedo, and surface albedo are obtained at four wavelengths from AERONET in each measurement, three different spectral regions are simulated with the libRadtran model. For computations in the UV range (280-400 nm), the AERONET retrievals of aerosol asymmetry factor, aerosol single scattering albedo, and surface albedo at 440 nm are used. The AERONET retrievals at 675 nm of the same variables are used in the visible range (400-700 nm), while in the near-infrared region (700-2800 nm) we used the average properties retrieved at 870 and 1020 nm. In each interval, these properties are considered as wavelength independent. This choice to perform the radiative transfer simulations is proven as adequate in the Appendix A. Other options in the model set-up are: extraterrestrial irradiance values are taken from Gueymard (2004); profiles of temperature, air density, ozone and other atmospheric gases are taken from the midlatitude summer/winter standard atmospheres; and

the radiative equation solver is the improved version of the discrete ordinate method of Stamnes et al. (2000) (DISORT2) calculated by 16-streams (e.g., de Miguel et al., 2011). After computing the solar irradiance in the different spectral intervals, the SW irradiance is evaluated by adding up the contributions of these three spectral regions.

In order to evaluate the aerosol radiative effect, the simulations under aerosol-free conditions are also computed with the same inputs as explained above, but with a fixed β value of 0.001.

The use of radiative transfer models fed with reliable experimental aerosol data to determine the ARE has been also employed in other studies (e.g., Barja and Antuña, 2011; Valenzuela et al.,2012; García et al., 2014).

Once the simulated radiometric values are obtained, ARE is derived for each interval (X represents UV, VIS, NIR, and SW) at the surface by:

$$ARE_X = \left(X^{\downarrow}_{aer} - X^{\uparrow}_{aer}\right) - \left(X^{\downarrow}_{NOaer} - X^{\uparrow}_{NOaer}\right) \quad (1)$$

where X_{aer} and X_{NOaer} are the irradiances (W m^{-2}) for the X range under actual and aerosol-free conditions, respectively.

Daily values are obtained by the integration of the hourly data during the whole day (24 h) considering ARE = 0 Wm^{-2} for SZA > 90º (e.g., Bush and Valero, 2003; Valenzuela et al., 2012) and assuming cloud-free conditions along the day:

$$ARE_{daily} = \sum ARE_{hourly} \frac{dt}{24} \quad (2)$$

The aerosol forcing efficiency (AFE) is defined as the rate at which the radiative effect varies per unit of AOD (e.g., Di Biagio et al., 2009; and the references therein). The linear relationship between aerosol radiative effect and AOD is well known (see, e.g., Costa et al., 2004, 2006; Di Biagio et al., 2009). Hence, in this study, ARE is obtained as the slope of linear fits in the ARE vs AOD_{500nm} relationships. Therefore, AFE values are expressed in W m^{-2} per AOD_{500nm}-unit ($Wm^{-2}\tau^{-1}$).

With respect to the temporal trends calculated in this study, the Sen's method (Sen, 1968) is applied to evaluate the slope of a time series using the Mann-Kendall non parametric test to determine the significance of these rates. The Sen's method is not greatly affected by outliers and can be computed when there are gaps in the database (Collaud Coen et al., 2013). This is a common and adequate method in temporal trend evaluation (e.g., Sánchez-Lorenzo et al., 2013). The trends calculated in this study are obtained in the corresponding physical units per year. However, to unify notation with previous studies dealing with the radiative effect trends of clouds and aerosols (e.g., Mateos et al., 2013b), the results are multiplied by 10 and expressed in physical units per decade. In this way, the trends are also easier to read.

4. Analysis of aerosol properties over the Iberian Peninsula

A direct CIMEL retrieval (AOD at 440 nm) is selected to perform the climatological analysis because the estimations of AOD_{500nm} (used in the ARE calculations) are obtained using α values. Hence, we minimized the impact of other uncertainty sources in the AOD analysis. Besides, the results for AOD_{440nm} and AOD_{500nm} do not differ excessively. In order to identify the differences in the aerosol climatology over the six sites analyzed in this study, the monthly distribution of the

daily values of the AOD_{440nm} and α are evaluated using the database mentioned in Table 1. All the available level 2.0 AERONET measurements are used in this section.

Figure 1 shows the climatology of the aerosol load by box whisker plots. Several conclusions can be drawn from this figure. The highest values of the AOD occur in Barcelona, as can be expected because it is a large city. With respect to the monthly average values (triangles in the figure), the central stations in the Iberian Peninsula (Palencia and Évora) exhibit AOD_{440nm} below 0.2, while the southern sites (Cabo da Roca, Granada, and El Arenosillo) show aerosol load over 0.2 during summer months. The AOD_{440nm} seasonal distribution is seen, with maximum values in summer and minimum ones in winter. However, the seasonality becomes more evident in the stations outside the central area of the Iberian Peninsula. The large differences between median and average values for some months evidence a large impact of high aerosol optical depth events on the monthly climatology. In this line, the bimodality of the monthly AOD climatology (with two maximum monthly means occurring in March and summer months) observed for the El Arenosillo site has been already reported by previous studies (e.g., Bennouna et al., 2011), and directly attributed to desert dust intrusions from the African continent.

To go further in the characterization, α allows for a better understanding of the particle size over each site. Figure 2 shows the climatology of this variable over the six stations using also box whisker plots. Analyzing the monthly average means, α values larger than one, indicative of the predominance of fine particles, are dominant over Barcelona, Palencia, and Évora. The other three stations (Cabo da Roca, Granada, and El Arenosillo) present monthly α averages over and below 1, which means a larger variety of aerosol sizes over these stations. A seasonal dependence over Granada site is seen, with winter months dominated by fine particles and summer months by larger ones (see also Navas-Guzman et al., 2013). Values of α present a large variability during summer which is indicative of the influence of different aerosol types including biomass burning events and

252 Saharan dust transport (e.g., Pérez-Ramírez, 2008). The monthly distribution of α is symmetric with
253 similar average and median values through the year for the six sites.

254 With the daily AOD and α values, it is possible to classify the origin of the aerosol particles.
255 Previous studies suggest different thresholds of AOD and α (e.g., Hess et al., 1998; Pace et al.,
256 2006; Toledano et al., 2007b). A simple classification, which can be used for the whole Iberian
257 Peninsula, of aerosol type is carried out in this study. The threshold between fine and large particles
258 is placed at $\alpha = 1$, while the situations with a high aerosol load are those with $AOD_{440nm} > 0.2$.
259 Therefore, aerosol particles can be classified in four types: maritime ($AOD_{440nm} < 0.2$ and $\alpha < 1$),
260 desert dust ($AOD_{440nm} > 0.2$ and $\alpha < 1$), continental clean ($AOD_{440nm} < 0.2$ and $\alpha > 1$), and
261 continental polluted ($AOD_{440nm} > 0.2$ and $\alpha > 1$). Note that the limit of $AOD_{440nm} < 0.2$ is arbitrary
262 and this value could be adjusted according to the sites, which likely produce a different distribution
263 in the pie diagrams. Actually, even close stations can present slight differences in the α-AOD
264 classification (see, e.g., Obregón et al. 2012). However it is not the aim of this work to provide an
265 extensive aerosol climatology, but rather to demonstrate the great variety of air masses over Iberia
266 which transport different aerosol types. Although other types, such as biomass burning or mixed
267 aerosols, are placed in the boundaries of these types, this simple classification can provide
268 information about the aerosol sources for the six sites. The classification used here is in line with
269 the previous studies. For instance, Toledano et al., (2007b) proposed for El Arenosillo site similar
270 thresholds (see their Table V), although they identified continental polluted aerosols with an
271 AOD_{440nm} larger than 0.35 and $\alpha > 1.4$. Pace et al., (2006) proposed at Lampedusa island (Central
272 Mediterranean) a desert dust identification when $AOD_{440nm} \geq 0.15$ and $\alpha \leq 0.5$.

273 Figure 3 shows pie diagrams with the frequency of occurrence of the four aerosol types. The six
274 diagrams agree pointing at continental clean as the main type of aerosols over the Iberian Peninsula.
275 In Barcelona, there is also an important contribution of continental polluted, since Barcelona is a

large coastal city with relevant pollution levels from vehicular and ship traffic (e.g., Reche et al., 2011). The influence of maritime aerosols is notable at El Arenosillo, Cabo da Roca, and Évora sites (see also e.g., Bennouna et al., 2011; Obregón et al., 2012). Furthermore, desert dust events are shown to be common in the Iberian Peninsula with a higher occurrence at Granada and El Arenosillo sites (the two closest points to the African continent and hence to the Saharan desert) (see also Toledano et al., 2007b; Guerrero-Rascado et al., 2009; Antón et al., 2012). For instance, the minimum values of α obtained for Granada station during summer months are linked to the higher likelihood of desert dust events (Valenzuela et al., 2012), being sometimes associated with high aerosol loads (Córdoba-Jabonero et al., 2011). These results corroborate the findings obtained by previous studies about desert dust events over the Iberian Peninsula (see, e.g., Lyamani et al., 2005; Toledano et al., 2007b; Cachorro et al., 2008).

The temporal trend of aerosol load can be established over the last decade in the Iberian Peninsula. The yearly values of AOD_{440nm} at the six sites are shown in Figure 4. The geographical distribution of AOD through the Spanish geography is observed in the figure. Barcelona site presents yearly values over ~0.2. Granada, El Arenosillo, and Cabo da Roca exhibit yearly means in the interval between 0.15 and 0.22, while the means for Palencia and Évora sites are slightly lower in the range 0.12-0.18. Analyzing the six sites together, the year of 2010 presents one of the minimum values of AOD_{440nm}, while the maximum averages seem to appear at the early 2000s. The different sampling of AOD measurements in the six sites can produce discrepancies because different events are or are not captured in each database. In addition, possible technical problems and meteorological conditions (CIMEL aerosol data are recorded under cloud-free skies) cause a non-equally distribution through the year. Overall, summer is the season with the largest contribution of data, followed by spring, autumn, and winter. Looking at the years with a large sampling (>200 days in, at least, four stations), 2005, 2007, and 2011, all the features mentioned above are corroborated for these particular years. The minimum of 2010 occurs when two Southern sites (El Arenosillo and

301 Cabo da Roca) have not enough data to evaluate the yearly mean. Hence, we cannot ensure that the
302 apparent minimum of AOD recorded that year is linked to global-scale phenomena or to more local
303 conditions at the other sites. During 2010 a persistent negative phases of North Atlantic Oscillation
304 (NAO) and Quasi Biennal Oscillation (QBO) indexes was observed (e.g., Steinbrecht et al., 2011),
305 and the connection between air mass transport at global scale and particulate matter (at the surface)
306 is proved by Pey et al., (2013) in the Eastern Iberian Peninsula.

307 With respect to the temporal trend rates, the evolution of these yearly values seems to be weak. The
308 evaluation of the trend rates (see Section 3 for details) produces the more statistically significant
309 trend for the Barcelona site, where a decrease of the aerosol load of 0.09 AOD_{440nm}-unit per decade
310 is observed with a *p value* of 0.02. Évora and Palencia stations showed trend rates of -0.06 and -
311 0.04 AOD_{440nm}-unit per decade with *p values* of 0.06 and 0.10, respectively. The *p values* for the
312 other sites point out non-statistically significant trends. In spite of that, the sign of the temporal
313 trends is negative for all of them. Hence, a slight reduction of the aerosol load over the Iberian
314 Peninsula is observed since 2000. This result obtained in the Southeastern Europe is in line with the
315 long-term analysis of AOD series performed in Northern Germany and Switzerland by Ruckstuhl et
316 al. (2008). These authors highlight a strong decrease of aerosol load starting in 1985, while the
317 values are stabilized since about 2000.

318 The reasons behind the decrease in the aerosol load since the early 2000s are a mixed of
319 anthropogenic and natural sources. As was reported by Aas et al. (2013), the particulate matter
320 (PM) emissions in the Iberian Peninsula have decreased around 25% between 2000 and 2011.
321 Furthermore, observational PM data in different Spanish sites have also shown a decrease trend in
322 the 2000s (e.g., Barmpadimos et al., 2012; Cusack et al., 2012; Pey et al., 2013; Bennouna et al.,
323 2014; Mateos et al., 2014). This fact can be understood by the effect of the current economic crisis
324 and the implementation of new environmental laws to control the pollution (e.g., Querol et al.,

2014). In addition, recent studies have shown that natural aerosols have also decreased in the last decade. For instance, Gkikas et al. (2013) reported, using satellite AOD estimations, that strong and extreme desert dust episodes in the Mediterranean decreased in the period 2000-2007 over land surfaces. This trend is understood due to the low spring and summer frequencies in 2005 and 2007 and the high frequencies in 2000 and 2003. As it was shown by Pey et al. (2013), one possible reason behind this trend is the atypical trajectories followed by the air masses emerging from North Africa in summer since 2006. Hence, both columnar and surface aerosols have pointed out a decrease in the aerosol load over the Iberian Peninsula, which has increased solar radiation levels reaching the surface in the 2000s (Mateos et al., 2014).

5. Inter-annual and intra-annual evolution of ARE

From the daily data, the yearly ARE for each station and spectral range are evaluated to analyze their inter-annual changes (see Figure 5). In spite of the high variability of the yearly values with large standard deviations (see the vertical bars for Palencia station in the figure), the radiative effects of atmospheric aerosols have slightly declined over the last years. The patterns of ARE in the UV, VIS, NIR, and SW ranges are similar, since the inter-annual changes are simultaneously observed in the four spectral intervals. The significance levels of the temporal trends (Mann-Kendall nonparametric test at the 95% confidence interval) are evaluated. Évora and Palencia sites exhibit statistically significant trends in the periods 2005-2012 and 2003-2012, respectively. The trends for the aerosol effects for Palencia (Évora) are: +4.9 (+3.2) Wm^{-2} per decade in ARE_{SW}, +3.3 (+2.1) Wm^{-2} per decade in ARE_{VIS}, +0.1 (+0.08) Wm^{-2} per decade in ARE_{NIR}, and +0.06 (+0.03) Wm^{-2} per decade in ARE_{UV}. The *p values* of the trends for Évora site range between 0.009 and 0.019, while for Palencia site are between 0.02 and 0.03. The other four stations present positive trends in all the spectral ranges, but they are not statistically significant, at least, at the 95%

confidence interval. The decrease in the aerosol effects is in line with the previous fall in the AOD values in the 2000s mentioned in Section 4. Furthermore, this slight reduction in the radiative effects of the atmospheric aerosol over the Iberian Peninsula could partially contribute to the increase in the levels of SW radiation at the surface (the brightening phenomenon) in this region reported by Sanchez-Lorenzo et al. (2013) and Mateos et al. (2013b).

To establish the general behavior of the ARE over the whole Iberian Peninsula, the yearly values using the six ground-based stations are evaluated. Only those years with, at least, simultaneous measurements at three sites are considered in these averages, and consequently, the time period is limited to 2004-2012. Figure 6 shows the evolution of the ARE and AOD at 500 nm for the entire peninsula. The previously discussed reduction of aerosol load in the six individual datasets is again corroborated with the mean data series. This decline produces a consequent decrease in the aerosol radiative effect at the four spectral ranges. The temporal trends of these yearly values are evaluated, and all the trends resulted statistically significant at the 95% significance level are shown in Figure 6. Overall, ARE_{SW} over the Iberian Peninsula increased 3.6 W m^{-2} per decade while the aerosol reduced 0.04 AOD_{500nm}-unit per decade. The yearly aerosol radiative effects over the entire peninsula are in the ranges: $-1.1 < ARE_{UV} < -0.7$ W m^{-2}, $-5.7 < ARE_{VIS} < -3.5$ W m^{-2}, $-2.6 < ARE_{NIR} < -1.6$ W m^{-2}, and $-8.8 < ARE_{SW} < -5.7$ W m^{-2}. The larger contribution of the visible spectral region with respect to the whole solar spectrum was also noticed by Bush and Valero (2003), and this is expected since the maximum of shortwave radiation is found in this interval. The relationship between ARE and AOD_{500nm} is analyzed more in detail in Section 6, when the aerosol forcing efficiency is evaluated for each ground-based station.

In addition to the inter-annual changes, the intra-annual behavior is also analyzed. For this purpose, the annual cycle (12 monthly means) is evaluated for the six stations (see Figure 7). A seasonal pattern is seen in ARE_{UV} and ARE_{VIS}, and therefore, ARE_{SW}. However, ARE_{NIR} does not follow a

seasonal pattern, particularly at the Évora and Palencia stations given that ARE_{NIR} remains nearly constant. Small differences among the six stations are observed in the annual cycle during the cold seasons. The aerosol radiative effects are stronger during summer months. This can be related to the higher likelihood of desert dust or biomass burning events over the Iberian Peninsula in these months (e.g., Cachorro et al., 2008; Valenzuela et al., 2012), as was mentioned above. This is corroborated by the increase of the differences among the stations during the warm season, likely due to the variability in the impact of the desert dust episodes which strongly depend on the geographical location of each site. The higher occurrence of large aerosol loads during the warm seasons (see Figure 1), can explain the more negative ARE during summer and spring in Figure 7. For instance, the Barcelona station, with the largest values of AOD_{440nm}, is the bottom curve of each panel in Figure 7. Furthermore, the influence of mineral dust aerosol (with high aerosol optical depth) during these months also causes strong radiative effects, as was also reported by previous studies (e.g., Cachorro et al., 2008; Guerrero-Rascado et al., 2009; Antón et al., 2011; Román et al., 2013; García et al., 2014). In addition, the bimodality of the monthly AOD climatology mentioned in Section 4 has its impact on the radiative effects. The annual AOD cycle (see Figure 1, El Arenosillo site) causes the inverse monthly distribution of ARE with a first minimum in March. This effect is more clearly seen in ARE_{NIR} and ARE_{SW}.

6. Aerosol radiative forcing efficiency in different spectral ranges

The daily AFE values are calculated (following the methodology described in Section 3) in all the spectral ranges. AFE is a function of the aerosol optical properties, where both the aerosol particle size distribution and absorptive properties play a key role (e.g., Antón et al., 2011). As we assumed a fixed value of SSA = 0.90 in the simulations with $AOD_{440nm} < 0.15$ (see Table 2), the AFE is calculated only for those cases showing AOD_{440nm} larger than 0.15.

To identify the influence of SSA and α on AFE, this variable is calculated for several intervals of each aerosol property. Four categories of single scattering albedo at 675 nm are established in the calculation of the AFE: $1.0 \geq SSA_1 > 0.95$, $0.95 \geq SSA_2 > 0.90$, $0.90 \geq SSA_3 > 0.85$, and $0.85 \geq SSA_4 > 0.80$. Furthermore, aerosol size is classified in three intervals: $0 \leq \alpha_1 \leq 1$, $1 < \alpha_2 \leq 1.5$, and $1.5 < \alpha_3 \leq 2$. Note that two intervals in the range of α larger than 1 have been considered. One for median particles and another one for fine particles, because of the relevant importance of median size particle (continental or mixed aerosol aerosols types) over the Iberian Peninsula (see Figure 3). Although the general classification between fine and coarse particles requires a more refined classification (Schuster et al.,2006; Prats et al., 2011), the more general intervals selected in this study are adequate to perform a study of the aerosol sizes at the six stations together.

Figure 8 shows the AFE obtained for the UV (AFE_{UV}), VIS (AFE_{VIS}), NIR (AFE_{NIR}), and SW (AFE_{SW}) ranges for all these intervals. The threshold to evaluate the average in each sub-interval is fixed at 10 data points. From these figures it is seen that, the stronger the absorption by aerosols, the stronger their forcing efficiency. That is a decrease in the absolute values of the AFE for increasing SSA and for all particle size. In general, the groups of non-absorbing particles exhibit a good agreement among the six stations (see, for instance, AFE values in all the spectral ranges in the interval $1 < \alpha \leq 1.5$). Larger differences are obtained in the case of more absorbing aerosol particles. These can be understood because of the different types of aerosols presented over each site (see Section 4) and the different data numbers. The average AFE values over the whole Iberian Peninsula (considering the six stations together) are presented in Table 3 as a function of α and SSA, separately. The role played by the aerosol size on AFE values is different in the three sub-intervals of the shortwave radiation. AFE_{UV} and AFE_{VIS} are larger (in absolute value) for fine particles, while the opposite occurs in the case of AFE_{NIR}. As a result of these mixed effects, AFE_{SW} shows also a decrease in its values with increasing α, but this effect is weaker than for the visible and ultraviolet parts. SSA exhibits a more dominant role. As was observed before, the most

422 negative values are achieved for the most absorbing aerosols considered in this study (group 1 of
423 SSA, see Table 3).

424 The average values of forcing efficiency obtained in this study (see Table 3) are in line with those
425 found by other authors. Table 4 summarizes the results obtained by previous studies. It is difficult to
426 assess some features in the comparison with previous reported AFE values, because of the different
427 aerosol types, time periods and methods that are analyzed. Our study presents the evaluation of
428 ARE with six long-term databases of aerosol properties. In spite of that, the values shown in Table
429 3 agree with those of Table 4, but the larger discrepancies are observed with the studies focusing on
430 specific events. Our results match better with the results reported by, e.g., Zhou et al. (2005),
431 Meloni et al. (2005), and Di Biagio et al. (2010). As was noticed by, e.g., Costa et al. (2004, 2006)
432 and Di Biagio et al. (2010), AFE at the surface is larger (in absolute term) for aerosols characterized
433 by smaller and absorbing particles. This result is corroborated by the findings shown in this study.
434 Furthermore, as was pointed out by Di Biagio et al. (2010), the aerosol absorption is the dominant
435 factor on AFE evaluated at the surface.

436 To evaluate the contribution of each spectral range with respect to the shortwave, the dependence of
437 each AFE ratio (VIS to SW and NIR to SW) on SSA and α is shown in Figure 9. AFE_{VIS}/AFE_{SW}
438 and AFE_{NIR}/AFE_{SW} ratios are shown in the figure since their contributions are the dominant.
439 AFE_{UV}/AFE_{SW} ratio can be obtained as 100% minus the sum of the percentage of the two other
440 ranges. As expected, non substantial differences are observed in the behavior of the six stations
441 considered in this study. The NIR contribution becomes more decisive for large particles ($\alpha < 1$). It
442 is expected that larger particles interact more with the longer wavelengths, while the smaller
443 particles present more interaction with the shorter wavelengths. The presence of large particles with
444 low SSA (high absorption) leads to a reduction of the AFE_{NIR}/AFE_{SW} ratio as well as an increase of
445 the AFE_{VIS}/AFE_{SW} ratio. However, for non-absorbing (high SSA) large particles, the

446 AFE_{NIR}/AFE_{SW} ratio increases, and the contributions of the visible and infrared parts become more
447 similar (both around ~40-50%). The difference between AFE_{VIS}/AFE_{SW} and AFE_{NIR}/AFE_{SW}
448 increases for intermediate - fine particles. For these particles, the AFE_{VIS}/AFE_{SW} ratio does not
449 show a dependence on SSA. The smallest contribution of the NIR interval is around ~25% under
450 strong absorbing aerosols and fine particles, while AFE_{VIS}/AFE_{SW} is still over 60%. For this case,
451 the contribution of the ultraviolet range achieves a maximum of ~15%, being almost comparable
452 with the near infrared contribution. In summary, aerosol size determines the relevance of VIS-NIR
453 ranges, while SSA plays a key role, particularly, for large particles.

454

455 **7. Conclusions**

456 Six long-term datasets of aerosol properties over the Iberian Peninsula were analyzed and used as
457 input in a radiative transfer model to simulate ultraviolet, visible, near-infrared, and shortwave
458 radiation. The aerosol radiative effect (ARE) and aerosol forcing efficiency (AFE) were calculated.
459 The main conclusions are as follows:

460 1) The annual cycles of AOD and α values of atmospheric aerosols over the six analyzed stations
461 present high variability among them, emphasizing the inhomogeneity of the Iberian Peninsula,
462 mainly due to the different aerosol types over each station. The Barcelona site presents the largest
463 values of AOD, although Southern stations (Granada and El Arenosillo sites) frequently exhibit
464 daily values over 0.2 during summer months. The classification α-AOD has shown that continental
465 (mainly, clean) is the principal type of aerosol over the Iberian Peninsula. However, maritime
466 aerosols are also common in the Cabo da Roca, El Arenosillo and Évora sites. Desert dust events
467 are registered at the six sites, with the highest frequency at Granada and El Arenosillo, but the most
468 relevant feature is the South-North gradient of desert dust load which modulates the aerosol
469 climatology over the Iberian Peninsula.

2) The aerosol load over the Iberian Peninsula has shown a decrease trend between 2004 and 2012 (-0.04 per unit of AOD_{500nm} per decade, being statistically significant at the 95% of significance level). Yearly values of the AOD at 440 nm have also shown a statistically significant trend of -0.09 AOD_{440nm}-unit per decade at Barcelona site. The temporal trends for the rest of the stations are not statistically significant at the 95% significance level, but all of them are negative. Hence, a reduction of the aerosol column load over the Iberian Peninsula is observed in the last decade.

3) In the whole Iberian Peninsula, yearly ARE_{UV} ranges between -1.1 and -0.7 Wm^{-2}, ARE_{VIS} ranges between -5.7 and -3.6 Wm^{-2}, and ARE_{NIR} has values between -2.6 and -1.6 Wm^{-2}. As a result, ARE_{SW} is in the range between -8.8 and -5.7 Wm^{-2}. The temporal trends of ARE_{UV}, ARE_{VIS}, ARE_{NIR}, and ARE_{SW} exhibit positive statistically significant trends between 2004 and 2012. For instance, the trend rate for the ARE_{SW} is +3.6 Wm^{-2} per decade (statistically significant at the 95% of significance level).

4) The intra-annual ARE cycle exhibits larger values during the spring and summer months when the likelihood of high aerosol loading over the Iberian Peninsula increases. In general, the annual AOD cycle is driven by the occurrence of Saharan dust events.

5) The AFE values at the six stations used in this study are in good agreement. Conditions of high α (small particles predominate) and low SSA (high absorption) lead to the largest negative AFE values. Overall, as an average for the Iberian Peninsula: AFE_{UV} = -6 $Wm^{-2}\tau^{-1}$, AFE_{VIS} = -34 $Wm^{-2}\tau^{-1}$, AFE_{NIR} = -19 $Wm^{-2}\tau^{-1}$, and AFE_{SW} = -59 $Wm^{-2}\tau^{-1}$.

6) The contribution of the ultraviolet, visible, and infrared to total shortwave aerosol forcing efficiency is governed by the aerosol type. In general, the visible part of the spectrum is the most dominant part. Non-absorbing large particles cause a more equal contribution of VIS and NIR intervals, while the UV range shows a higher contribution for absorbing fine particles.

Appendix A

The two choices in the performance of radiative transfer simulations from the libRadtran code concerning aerosol properties are justified in this section.

First at all, as it is mentioned in the text, most of the data present $AOD_{440nm} < 0.15$ (~70% for Palencia, Granada, and Évora sites). For these low values, SSA = 0.9 and g = 0.75 are selected by the representativeness of the local aerosols in the six sites of study (e.g., Cachorro et al., 2010). To analyze possible uncertainties emerging from this choice, the radiative net fluxes are also evaluated for SSA and g values covering the most variety of aerosols observed in the Iberian Peninsula. Hence, $SSA_1 = 0.8$, $SSA_2 = 1.0$, $g_1 = 0.65$, and $g_2 = 0.80$ are selected in this analysis. Four possibilities or scenarios are simulated mixing the two values of the aerosol properties. The radiation obtained in each scenario is compared with the assumed case of SSA = 0.9 and g = 0.75. The two optical properties are also fixed as non-wavelength-dependent in this analysis. The AOD_{440nm} used is 0.15, the worst scenario possible for these cases because the higher the AOD the stronger the impact of aerosol properties. The simulations are performed for the four spectral ranges. Table A1 shows the mean relative difference observed for the four scenarios and two different SZAs (30º and 60º). The assumption considered in this study causes, in the worst possible scenarios, errors in the ARE retrievals (obtained as the expanded errors from the radiative uncertainty) < 10%, < 6%, < 3%, and < 5% for the UV, VIS, NIR, and SW ranges, respectively. As the cases with $AOD_{440nm} < 0.15$ are the large majority of the Iberian Peninsula, they should be included in the study. The aerosol characterization, with respect to SSA or g, for these 'clean' cases present large uncertainties itself, and no reliable information is extracted from them. Hence, the results of this sensitivity study are adequate. As the SSA influences the diffuse radiation, the worst

517 results are obtained at large SZAs. The impact of g on the net fluxes is very weak. In conclusion,
518 the choice of SSA = 0.9 and g = 0.75 in a clean scenario (AOD_{440nm} < 0.15) is proven as adequate
519 because of two reasons: a) representativeness of the local aerosols which can be mixture of different
520 types, and b) the low uncertainty produced in the simulations by SSA and g under these conditions.

521 The choice of fixed SSA and g values within each of the spectral ranges (UV, VIS, and NIR)
522 represented by the CIMEL spectral measurements is also justified here. The aerosol models by
523 Shettle (1989) included in the libRadtran code (see Mayer and Kylling, 2005) are used to evaluate
524 the uncertainty of using this approximation. The continental clean aerosols (most common type in
525 the Iberian Peninsula, see Figure 3), and continental polluted aerosols (also very common, which
526 present an extreme case of absorption) are tested in this analysis. The simulations are performed for
527 the expected spectral behavior of SSA and g following Shettle (1989) and the case of fixed
528 properties in the UV (SSA and g values at 440 nm), VIS (SSA and g values at 675 nm), and NIR
529 intervals (SSA and g average of values at 870 and 1020 nm). Figure A1 presents the evolution of
530 the relative error (considering as reference the net flux with the expected spectral dependence of
531 aerosol properties) for several AOD values between aerosol-free and AOD_{550nm} = 0.6. In the case of
532 continental clean aerosols (Figure A1.a), the error of using our assumption is lower than 5% for all
533 SZAs and spectral ranges. Therefore, as the large majority of aerosol particles are of this type, the
534 methodology used and proposed in this study only introduces a relative error below 5% in the
535 majority of the simulations. With respect to the continental polluted aerosols (Figure A1.b), the
536 error increases achieving a maximum around 20% for the UV range and very turbid conditions. For
537 large AOD conditions in the Iberian Peninsula (e.g., AOD_{550nm} = 0.4) but with low frequency of
538 occurrence in contrast to AOD_{440nm} < 0.15, the error of the SW range is below 5%. However, the
539 UV range is more sensitive to our method and the error is around 15% at SZA = 60º. As it was
540 mentioned above, the errors are larger for large SZAs because of the possible interaction between
541 absorption and scattering processes resulting the diffuse radiation. The visible range is more

sensitive to the spectral variations than the NIR interval, which exhibits a maximum error around 11% at SZA = 60º and AOD_{550nm} = 0.6. The daily net radiative fluxes are also evaluated for the two aerosol types in order to quantify the uncertainty in the final simulated data used in this study. For Palencia site (and the corresponding SZA evolution), a daily value for the June 20th is simulated assuming TOC = 300 DU and PWC = 1 cm. The results for the continental polluted case with AOD_{440nm} = 0.4 exhibit differences between the spectral and fixed-band aerosol properties of: 7.5%, 5.3%, 4.0%, and 4.8% for the UV, VIS, NIR, and SW intervals. The relative errors for the same intervals with continental clean (and same AOD value) are: 1.9%, 1.2%, 1.4%, and 1.4%, respectively. Therefore, the uncertainty due to fixed optical properties in each spectral range is dependent on the aerosol type but the error caused can be considered as acceptable. Since actual aerosols often present mixtures of different types, the uncertainty of using the theoretical spectral evolution for one type (given by an aerosol model) can also produce uncertainties which should be taken into account. Although other aerosol types are not tested in this analysis, a similar behavior can be expected. For instance, for the case of desert dust aerosols, Román et al. (2013) found a slight influence of spectral aerosol absorption properties on UV irradiance analyzing a strong Saharan intrusion over Granada site.

Therefore, the two assumptions performed in this study in the simulations are adequate for the evaluation of net fluxes and aerosol radiative effects. The uncertainties that can be introduced in the daily values are acceptable being around or smaller than 5% for the net SW radiation. This uncertainty is usually achieved in clear-sky modeling (e.g., Mateos et al., 2013a).

Acknowledgments

The work is supported by the Spanish Ministry of Science and Technology (currently MINECO) through projects CGL2010-18782, CSD2007-00067, CGL2011-29921-C02-01, CGL2011-23413,

566 CGL2011-24891, CGL2011-13085-E, CGL2011-13580-E, CGL2012-33576, and CGL2012-
567 33576; FEDER (Programa Operacional Factores de Competitividade - COMPETE). Also by
568 Portuguese funding through FCT - Fundação para a Ciência e a Tecnologia in the framework of
569 project FCOMP-01-0124-FEDER-009303 (PTDC / CTE-ATM / 102142 / 2008); the Évora
570 Geophysics Centre, Portugal, under the contract with FCT, PEst-OE/CTE/UI0078/2014; and the
571 Andalusia Regional Government through projects P08- RNM-3568 and P10-RNM-6299. The
572 research leading to these results has received also funding from the European Union Seventh
573 Framework Programme (FP7/2007-2013) under grant agreement Nr. 262254 [ACTRIS]. Manuel
574 Antón and Carlos Toledano thank Ministerio de Ciencia e Innovación and Fondo Social Europeo
575 for the awards of a postdoctoral grant (Ramón y Cajal), and Mar Sorribas for postdoctoral grant
576 (Juan de la Cierva). We must specially thank the AERONET-GSFC, PHOTONS-LOA and RIMA-
577 GOA-UVa staff for their scientific and technical support. Ozone Monitoring Instrument (OMI) and
578 Total Ozone Mapping Spectrometer (TOMS) ozone column data were obtained from the Giovanni
579 online data system, developed and maintained by the NASA GES DISC.

580

581 **References**

582 Aas, W., Espen Yttri, K., Stohl, A., Lund Myhre, C., Karl, M., Tsyro, S., Marečková, K.,
583 Wankmüller, R., Klimont, Z., Heyes, C., Alastuey, A., Querol, X., Pérez, N., Moreno, T.,
584 Lucarelli, F., Areskoug, H., Balan, V., Cavalli, F., Putaud, J.P., Cape J.N., Catrambone, M.,
585 Ceburnis, D., Conil, S., Gevorgyan, L., Jaffrezo, J.L., Hueglin, C., Mihalopoulos, N.,
586 Mitosinkova, M., Riffault, V., Sellegri, K., Spindler, G., Schuck, T., Pfeffer, U., Breuer, L.,
587 Adolfs, D., Chuntonova, L., Arabidze, M., and Abdulazizov, E.: Transboundary particulate
588 matter in Europe Status report 2013, EMEP Report, 4/2013 (Ref. O-7726), ISSN: 1504-6109
589 (print), 1504-6192 (online), 2013.

590 Antón, M., Gil, J.E., Fernández-Gálvez, J., Lyamani, H., Valenzuela, A., Foyo-Moreno, I., Olmo, F.
591 J., and Alados-Arboledas, L.: Evaluation of the aerosol forcing efficiency in the UV erythemal
592 range at Granada, Spain, J. Geophys. Res., 116, D20214, doi:10.1029/2011JD016112, 2011.

593 Antón, M., Valenzuela, A., Cazorla, A., Gil, J.E., Fernández-Gálvez, J., Lyamani, H., Foyo-
594 Moreno, I., Olmo, F.J., Alados-Arboledas, L.: Global and diffuse shortwave irradiance during a
595 strong desert dust episode at Granada (Spain), Atmos. Res., 118, 232–239,
596 doi:10.1016/j.atmosres.2012.07.007, 2012.

597 Antón, M., Valenzuela, A., Mateos, D., Alados, I., Foyo-Moreno, I., Olmo, F.J., Alados-Arboledas,
598 L.: Lonwave aerosol radiative effects during an extreme desert dust event in Southeastern
599 Spain, Atmos. Res., doi: 10.1016/j.atmosres.2014.05.022, 2014.

600 Barja, B., and Antuña, J.C.: The effect of optically thin cirrus clouds on solar radiation in
601 Camagüey Cuba. Atmos. Chem. Phys., 11, 8625–8634, doi:10.5194/acp-11-8625-2011, 2011.

602 Barmpadimos, I., Keller, J., Oderbolz, D., Hueglin C., and Prèvôt, A.S.H.: One decade of parallel
603 fine ($PM_{2.5}$) and coarse (PM_{10}- $PM_{2.5}$) particulate matter measurements in Europe: trends and
604 variability, Atmos. Chem. Phys. 12, 3189-3203, doi: 10.5194/acp-12.3189-2012, 2012.

605 Bennouna, Y., Cachorro, V., Toledano, C., Berjón, A., Prats, N., Fuertes, D., Gonzalez, R.,
606 Rodrigo, R., Torres, B., and de Frutos, A.: Comparison of atmospheric aerosol climatologies
607 over southwestern Spain derived from AERONET and MODIS, Rem. Sen. Env. 115, 1272-
608 1284, 2011.

609 Bennouna, Y.S., Cachorro, V., Burgos, M.A., Toledano, C., Torres, B., and de Frutos, A.:
610 Relationships between columnar aerosol optical properties and surface Particulate Matter
611 observations in north-central Spain from long-term records (2003-2011), Atmos. Meas. Tech.
612 Discuss., 7, 5829-5882, doi:10.5194/amtd-7-5829-2014, 2014.

613 Boucher, O., Randall, D., Artaxo, P., Bretherton, C., Feingold, G., Forster, P., Kerminen, V.-M.,
614 Kondo, Y., Liao, H., Lohmann, U., Rasch, P., Satheesh, S.K., Sherwood, S., Stevens, B., and
615 Zhang, X.Y.: Clouds and aerosols. In Climate Change 2013: The Physical Science Basis.
616 Contribution of Working Group I to the Fifth Assessment Report of the Intergovernmental
617 Panel on Climate Change. T.F. Stocker, D. Qin, G.-K. Plattner, M. Tignor, S.K. Allen, J.
618 Doschung, A. Nauels, Y. Xia, V. Bex, and P.M. Midgley, Eds. Cambridge University Press,
619 571-657, 2013.

620 Bush, B. C., and Valero, F. P. J.: Surface aerosol radiative forcing at Gosan during the ACE– Asia
621 campaign, J. Geophys. Res., 108(D23), 8660, doi:10.1029/2002JD003233, 2003.

622 Cachorro, V. E., Toledano, C., Prats, N., Sorribas, M., Mogo, S., Berjón, A., Torres, B., Rodrigo,
623 R., de la Rosa, J., and De Frutos, A. M.: The strongest desert dust intrusion mixed with smoke
624 over the Iberian Peninsula registered with Sun photometry, J. Geophys. Res., 113, D14S04,
625 doi:10.1029/2007JD009582, 2008.

626 Cachorro, V. E., Toledano, C., Antón, M., Berjón, A., de Frutos, A., Vilaplana, J. M., Arola, A., and
627 Krotkov, N. A.: Comparison of UV irradiances from Aura/Ozone Monitoring Instrument
628 (OMI) with Brewer measurements at El Arenosillo (Spain) – Part 2: Analysis of site aerosol
629 influence, Atmos. Chem. Phys., 10, 11867-11880, doi:10.5194/acp-10-11867-2010, 2010.

630 Collaud Coen, M., Andrews, E., Asmi, A., Baltensperger, U., Bukowiecki, N., Day, D., Fiebig, M.,
631 Fjaeraa, A. M., Flentje, H., Hyvärinen, A., Jefferson, A., Jennings, S. G., Kouvarakis, G.,
632 Lihavainen, H., Lund Myhre, C., Malm, W. C., Mihapopoulos, N., Molenar, J. V., O'Dowd, C.,
633 Ogren, J. A., Schichtel, B. A., Sheridan, P., Virkkula, A., Weingartner, E., Weller, R., and
634 Laj, P.: Aerosol decadal trends – Part 1: In-situ optical measurements at GAW and IMPROVE
635 stations, Atmos. Chem. Phys., 13, 869-894, doi:10.5194/acp-13-869-2013, 2013.

636 Córdoba-Jabonero, C., Sorribas, M., Guerrero-Rascado, J.L., Adame, J.A., Hernández, Y.,
637 Lyamani, H., Cachorro, V., Gil, M., Alados-Arboledas, L., Cuevas, E., and de la Morena, B.:
638 Synergetic monitoring of Saharan dust plumes and potential impact on surface: a case study of
639 dust transport from Canary Islands to Iberian Peninsula, Atmos. Chem. Phys., 11, 3067-3091,
640 doi:10.5194/acp-11-3067-2011, 2011.

641 Costa, M. J., Levizzani, V., and Silva, A. M.: Aerosol Characterization and Direct Radiative
642 Forcing Assessment over the Ocean. Part II: Application to Test Cases and Validation. J. Appl.
643 Meteor., 43, 1818–1833, doi: http://dx.doi.org/10.1175/JAM2157.1, 2004.

644 Costa, M.J., Sohn, B.J., Levizzani, V., and Silva, A.M.: Radiative forcing of Asian dust determined
645 from the synergized GOME and GMS satellite data - A case study, J. Meteorol. Soc. Jpn.,
646 84(1), 85-95, doi: 10.2151/jmsj.84.85, 2006.

647 Cusack, M., Alastuey, A., Pérez, N., Pey, J., and Querol, X.: Trends of particulate matter ($PM_{2.5}$)
648 and chemical composition at a regional site in the Western Mediterranean over the last nine
649 years (2002-2010), Atmos. Env. 12, 8341-8357, doi: 10.5194/acp-12-8341-2012, 2012.

650 de Miguel, A., Mateos, D., Bilbao, J., and Román, R.: Sensitivity analysis of ratio between
651 ultraviolet and total shortwave solar radiation to cloudiness, ozone, aerosols and precipitable
652 water, Atmos. Res., 102, 136–144, doi:10.1016/j.atmosres.2011.06.019., 2011.

653 Di Biagio, C., di Sarra, A., Meloni, D., Monteleone, F., Piacentino, S., and Sferlazzo, D.:
654 Measurements of Mediterranean aerosol radiative forcing and influence of the single scattering
655 albedo, J. Geophys. Res., 114, D06211, doi:10.1029/2008JD011037, 2009.

656 Di Biagio, C., di Sarra, A., and Meloni, D.: Large atmospheric shortwave radiative forcing by
657 Mediterranean aerosols derived from simultaneous ground-based and spaceborne observations

658 and dependence on the aerosol type and single scattering albedo, J. Geophys. Res., 115,
659 D10209, doi:10.1029/2009JD012697, 2010.

660 di Sarra, A., Pace, G, Meloni, D., De Silvestri, L., Piacentino, S., and Monteleone, F.: Surface
661 shortwave radiative forcing of different aerosol types in the Mediterranean, Geophys. Res.
662 Lett., 35, L02714, doi:10.1029/2007GL032395, 2008.

663 di Sarra, A., Di Biagio, C., Meloni, D., Monteleone, F., Pace, G., Pugnaghi, S., and Sferlazzo, D.:
664 Shortwave and longwave radiative effects of the intense Saharan dust event of 25–26 March
665 2010 at Lampedusa (Mediterranean Sea), J. Geophys. Res., 116, D23209,
666 doi:10.1029/2011JD016238, 2011.

667 Díaz, A. M., García, O.E., Díaz, J.P., Expósito, F.J., Utrillas, M.P., Martínez-Lozano, J.A., Alados-
668 Arboledas, L., Olmo, F.J., Lorente, J., Cachorro, V., Horvath, H., Labajo, A., Sorribas, M.,
669 Vilaplana, J.M., Silva, A.M., Elias, T., Pujadas, M., Rodrigues, J.A., and González, J.A.:
670 Aerosol radiative forcing efficiency in the UV region over southeastern Mediterranean:
671 VELETA2002 campaign, J. Geophys. Res., 112, D06213, doi:10.1029/2006JD007348, 2007.

672 Dubovik, O., and King, M.D.: A flexible inversion algorithm for retrieval of aerosol optical
673 properties from Sun and sky radiance measurements, J. Geophys. Res., 105, 20673-20696,
674 2000.

675 Dubovik, O., Smirnov, A., Holben, B.N., King, M.D., Kaufman, Y.J., Eck, T.F., and Slutsker, I.:
676 Accuracy assessments of aerosol optical properties retrieved from Aerosol Robotic Network
677 (AERONET) Sun and sky radiance measurements, J. Geophys. Res., 105, 9791-9806, 2000.

678 Dubovik, O., Sinyuk, A., Lapyonok, T., Holben, B.N., Mishchenko, M., Yang, P., Eck, T.F.,
679 Volten, H., Muñoz, O., Veihelmann, B., van der Zande, W.J., Leon, J.F., Sorokin, M., and

680 Slutsker, I.: Application of spheroid models to account for aerosol particle nonsphericity in
681 remote sensing of desert dust, J. Geophys. Res., 111, D11208, 2006.

682 Esteve, A.R., Estellés, V., Utrillas, M.P., and Martínez-Lozano, J.A.: Analysis of the aerosol
683 radiative forcing over a Mediterranean urban coastal site, Atmos. Res., 137, 194-204,
684 http://dx.doi.org/10.1016/j.atmosres.2013.10.009, 2014.

685 Foyo-Moreno, I., Alados, I., Antón, M., Fernández-Gálvez, J., Cazorla, A., and Alados-Arboledas,
686 L.: Estimating aerosol characteristics from solar irradiance measurements at an urban location
687 in Southeastern Spain, J. Geophys. Res. Atmos., 119, 1845–1859, doi:10.1002/2013JD020599,
688 2014.

689 García, O. E., Díaz, A. M., and Expósito, F. J.: Validation of AERONET estimates of atmospheric
690 solar fluxes and aerosol radiative forcing by ground-based broadband measurements, J.
691 Geophys. Res., 113, D21207, doi:10.1029/2008JD010211, 2008.

692 García, R.D., García, O.E., Cuevas, E., Cachorro, V.E., Romero-Campos, P.M., Ramos, R., and de
693 Frutos, A.M.: Solar radiation measurements compared to simulations at the BSRN Izaña
694 station: Mineral dust radiative forcing and efficiency study, J. Geophys. Res. Atmos., 119, 179–
695 194, doi:10.1002/2013JD020301, 2014.

696 Gkikas, A., Hatzianastassiou, N., Mihalopoulos, N., Katsoulis, V., Kazadzis, S., Pey, J., Querol, X.,
697 and Torres, O.: The regime of intense desert dust episodes in the Mediterranean based on
698 contemporary satellite observations and ground measurements, Atmos. Chem. Phys., 13,
699 12135-12154, doi:10.5194/acp-13-12135-2013, 2013.

700

701 Guerrero-Rascado, J.L., Olmo, F. J., Avilés-Rodríguez, I., Navas-Guzmán, F., Pérez-Ramírez, D.,
702 Lyamani, H., and Alados-Arboledas, L.: Extreme Saharan dust event over the southern Iberian

703 Peninsula in September 2007: active and passive remote sensing from surface and Satellite,
704 Atmos. Chem. Phys., 9, 8453–8469, doi:10.5194/acp-9-8453-2009, 2009.

705 Gueymard, C.: The sun's total and spectral irradiance for solar energy applications and solar
706 radiation models, Sol. Energy, 76, 423-453, 2004.

707 Hansen, J. E., Sato, M., Lacis, A., Ruedy, R., Tegen, I., and Matthews, E.: Climate forcings in the
708 industrial era, Proc. Natl. Acad. Sci. U.S.A., 95, 12753–12758, doi:10.1073/pnas.95.22.12753,
709 1998.

710 Hatzianastassiou, N., Katsoulis, B., and Vardavas, I.: Global distribution of aerosol direct radiative
711 forcing in the ultraviolet and visible arising under clear skies, Tellus B, 56, 51–71,
712 doi:10.1111/j.1600-0889.2004.00085.x, 2004.

713 Hess, M., Koepke, P., and Schult, I.: Optical Properties of Aerosols and Clouds: The Software
714 Package OPAC, Bull. Am. Meteorol. Soc., 79, 831-844, 1998.

715 Holben, B.N., Eck, T.F., Slutsker, I., Tanré, D., Buis, J.P., Setzer, A., Vermote, E., Reagan, J.A.,
716 KAufman, Y.J., Nakajima, T., Lavenu, F., Jankowiak, I., and Smirnov, A.: AERONET – A
717 federated instrument network and data archive for aerosol characterization, Rem. Sen. Environ.,
718 66, 1–16, 1998.

719 Horvath, H., Alados Arboledas, L., Olmo, F. J., Jovanovic, O., Gangl, M., Kaller, W., Sánchez, C.,
720 Sauerzopf, H., and Seidl, S.: Optical characteristics of the aerosol in Spain and Austria and its
721 effect on radiative forcing, J. Geophys. Res., 107(D19), 4386, doi:10.1029/2001JD001472,
722 2002.

723 Jayaraman, A., Lubin, D., Ramachandran, S., Ramanathan, V. , Woodbridge, E., Collins, W. D.,
724 and Zalpuri, K. S.: Direct observations of aerosol radiative forcing over the tropical Indian

725 Ocean during the Janauary–February 1996 pre-INDOEX cruise, J. Geophys. Res., 103, 13,827–
726 13,836, doi:10.1029/98JD00559, 1998.

727 Kazadzis, S., Kouremeti, N., Bais, A., Kazantzidis, A., and Meleti, C.: Aerosol forcing efficiency in
728 the UVA region from spectral solar irradiance measurements at an urban environment, Ann.
729 Geophys., 27, 2515–2522, doi:10.5194/angeo-27-2515-2009, 2009.

730 Lucht, W. and Roujean, J.L.: Consideration in parametric modelling of BRDF and albedo from
731 multi-angular satellite sensors observations, Remote Sens. Rev., 18, 343–379, 2000.

732 Lyamani, H., Olmo, F.J., and Alados-Arboledas, L.: Saharan dust outbreak over southeastern Spain
733 as detected by sun photometer, Atmos. Env., 39, 7276-7284,
734 doi:10.1016/j.atmosenv.2005.09.011, 2005.

735 Lyamani, H., Olmo, F. J., Alcántara, A., and Alados-Arboledas, L.: Atmospheric aerosols during
736 the 2003 heat wave in southeastern Spain II: Microphysical columnar properties and radiative
737 forcing, Atmos. Environ., 40, 6465–6476, doi:10.1016/j.atmosenv.2006.04.047, 2006.

738 Mallet, M., Dubovik, O., Nabat, P., Dulac, F., Kahn, R., Sciare, J., Paronis, D., and Leon, J.F.:
739 Absorption properties of Mediterranean aerosols obtained from multi-year ground-based
740 remote sensing observations, Atmos. Chem. Phys., 13, 9195-9210, doi:10.5194/acp-13-9195-
741 2013, 2013.

742 Mateos, D., Antón, M., Valenzuela, A., Cazorla, A., Olmo, F.J., and Alados-Arboledas, L.: Short-
743 wave radiative forcing at the surface for cloudy systems at a midlatitude site, Tellus B, 65,
744 21069, http://dx.doi.org/10.3402/tellusb.v65i0.21069, 2013a.

745 Mateos, D., Antón, M., Sanchez-Lorenzo, A., Calbó, J., and Wild, M.: Long-term changes in the
746 radiative effects of aerosols and clouds in a mid-latitude region (1985–2010), Global Planet.
747 Change, 111, 288-295, http://dx.doi.org/10.1016/j.gloplacha.2013.10.004, 2013b.

748 Mateos, D., Sanchez-Lorenzo, A., Antón, M., Cachorro, V.E., Calbó, J., Costa, M.J., Torres, B., and
749 Wild, M.: Quantifying the respective roles of aerosols and clouds in the strong brightening
750 since the early 2000s over the Iberian Peninsula, J. Geophys. Res. Atmos., 119, 10382–10393,
751 doi:10.1002/2014JD022076, 2014.

752 Mayer, B., and Kylling, A.: Technical note: The libRadtran software package for radiative transfer
753 calculations – description and examples of use, Atmos. Chem.Phys., 5, 1855–1877, 2005.

754 Meloni, D., di Sarra, A., DeLuisi, J., Di Iorio, T., Fiocco, G., Junkerman, W., and Pace, G.:
755 Tropospheric aerosols in the Mediterranean: 2. Radiative effects through model simulations and
756 measurements, J. Geophys. Res., 108(D10), 4317, doi:10.1029/2002JD002807, 2003.

757 Meloni, D., di Sarra, A., Di Iorio, T., and Fiocco, G.: Influence of the vertical profile of Saharan
758 dust on the visible direct radiative forcing, J. Quant. Spectrosc. Radiat. Transfer, 93, 397–413,
759 2005.

760 Moody, E.G., King, M.D., Platnick, S., Schaaf, C.B., and Gao, F.: Spatially complete global
761 spectral surface albedos: value-added datasets derived from Terra MODIS land products, IEEE
762 T. Geosci. Remote., 43, 144–158, 2005.

763 Navas-Guzmán, F., Bravo-Aranda, J.A., Guerrero-Rascado, J.L., Granados-Muñoz, M.J., and
764 Alados-Arboledas, L.: Statistical analysis of aerosol optical properties retrieved by Raman lidar
765 over Southeastern Spain, Tellus B, 65, 21234, http://dx.doi.org/10.3402/tellusb.v65i0.21234,
766 2013.

767 Nikitidou, E., Kazantzidis, A., De Bock, V., and De Backer, H.: The aerosol forcing efficiency in
768 the UV region and the estimation of single scattering albedo at a typical West European site,
769 Atmos. Env., 69, 313-320, doi:http://dx.doi.org/10.1016/j.atmosenv.2012.12.035, 2013.

770 Obregón M.A., Pereira S, Wagner F, Serrano A, Cancillo ML, Silva AM.: Regional differences of
771 column aerosol parameters in western Iberian Península, Atmos. Environ., 62, 208-219, doi:
772 10.1016/j.atmosenv.2012.08.016, 2012

773 Pace, G., di Sarra, A., Meloni, D., Piacentino, S., and Chamard, P.: Aerosol optical properties at
774 Lampedusa (central Mediterranean): 1. Influence of transport and identification of different
775 aerosol types, Atmos. Chem. Phys., 6, 697‑713, 2006.

776 Panicker, A. S., Pandithurai, G., Safai, P. D., and Kewat, S.: Observations of enhanced aerosol
777 longwave radiative forcing over an urban environment, Geophys. Res. Lett., 35, L04817,
778 doi:10.1029/2007GL032879, 2008.

779 Pérez-Ramírez, D., Aceituno, J., Ruiz, B., Olmo, F.J., and Alados-Arboledas, L.: Development and
780 calibration of a star photometer to measure the aerosol optical depth: Smoke observations at a
781 high mountain site, Atmos. Env. 42(11), 2733–2738, 2008.

782 Pey, J., Querol, X, Alastuey, A., Forastiere, F, and Stafoggia, M. African dust outbreaks over the
783 Mediterranean Basin during 2001–2011: PM_{10} concentrations, phenomenology and trends, and
784 its relation with synoptic and mesoscale meteorology, Atmos. Chem. Phys., 13, 1395-1410,
785 doi:10.5194/acp-13-1395-2013, 2013.

786 Prats, N., Cachorro, V.E., Berjón, A., Toledano, C., and De Frutos, A.M.: Column-integrated
787 aerosol microphysical properties from AERONET Sun photometer over south-western Spain.
788 Atmos. Chem. Phys. 11, 12353-12547, doi:10.5194/acpd-11-12353-2011, 2011.

789 Querol, X., Alastuey, A., Pandolfi, M., Reche, C., Pérez, N., Minguillón, M.C., Moreno, T., Viana,
790 M., Escudero, M., Orio, A., Pallarés, M., and Reina, F.: 2001-2012 trends of air quality in
791 Spain, Sci. Total Environ., 490, 957-969, 2014.

792 Rajeev, K., and Ramanathan, V.: Direct observations of clear-sky aerosol radiative forcing from
793 space during the Indian Ocean Experiment, J. Geophys. Res., 106, 17,221–17,235,
794 doi:10.1029/2000JD900723, 2001.

795 Reche, C., Viana, M., Moreno, T., Querol, X., Alastuey, A., Pey, J., Pandolfi, M., Prèvôt, A., Mohr,
796 C., Richard, A., Artiñano, B., Gomez-Moreno, F.J., and Cots, N.: Peculiarities in atmospheric
797 particle number and size-resolved speciation in an urban area in the western Mediterranean:
798 Results from the DAURE campaign, Atmos. Env., 45, 5282-5293,
799 doi:10.1016/j.atmosenv.2011.06.059, 2011.

800 Román, R., Antón, M., Valenzuela, A., Gil, J.E., Lyamani, H., de Miguel, A., Olmo, F.J., Bilbao, J.,
801 and Alados-Arboledas, L.: Evaluation of the desert dust effects on global, direct, and diffuse
802 spectral ultraviolet irradiance, Tellus B, 65, 19578,
803 http://dx.doi.org/10.3402/tellusb.v65i0.19578, 2013.

804 Román, R., Bilbao, J., and de Miguel, A.: Solar radiation simulations in the Iberian Peninsula:
805 Accuracy and sensitivity to uncertainties in inputs of a radiative transfer model, J. Quant.
806 Spectrosc. Ra., 145, 95-109, 2014.

807 Ruckstuhl, C., Philipona, R., Behrens, K., Coen M.C., Dürr, B., Heimo, A., Mätzler, C., Nyeki, S.,
808 Ohmura, A., Vuilleumier, L., Weller, M., Wehrli, C., and Zelenka, A.: Aerosol and cloud
809 effects on solar brightening and the recent rapid warming, Geophys. Res. Lett., 35, L12708,
810 doi:10.1029/2008GL034228, 2008.

811 Saha, A., Mallet, M., Roger, J. C., Dubuisson, P., Piazzola, J., and Despiau, S.: One year
812 measurements of aerosol optical properties over an urban coastal site: Effect on local direct
813 radiative forcing, Atmos. Res., 90, 195–202, doi:10.1016/j.atmosres.2008.02.003, 2008.

814 Sanchez-Lorenzo, A., Calbó, J., and Wild, M.: Global and diffuse solar radiation in Spain: Building
815 a homogeneous dataset and assessing trends, Global Planet. Change, 100, 343-352,
816 http://dx.doi.org/10.1016/j.gloplacha.2012.11.010, 2013.

817 Santos, D., Costa, M. J., and Silva, A. M.: Direct SW aerosol radiative forcing over Portugal,
818 Atmos. Chem. Phys., 8, 5771–5786, doi:10.5194/acp-8-5771-2008, 2008.

819 Schuster, G. L., Dubovik, O., and Holben, B. N.: Angstrom exponent and bimodal aerosol size
820 distributions, J. Geophys. Res., 111, D07207, doi:10.1029/2005JD006328, 2006.

821 Sen, P. K.: Estimates of the regression coefficient based on Kendall's tau, J. Am., Stat. Assoc., 63,
822 1379–1389, 1968.

823 Shettle, E. P.: Models of aerosols, clouds and precipitation for atmospheric propagation studies,
824 paper presented at Conference on Atmospheric Propagation in the UV, Visible, IR and MM-
825 Region and Related System Aspects, NATO Adv. Group for Aerosp. Res. and Dev.,
826 Copenhagen, 1989.

827 Stamnes, K., Tsay, S.C., Wiscombe, W., and Laszlo, I.: DISORT, a General-Purpose Fortran
828 Program for Discrete-Ordinate-Method Radiative Transfer in Scattering and Emitting Layered
829 Media: Documentation of Methodology, Tech. rep. Dept. of Physics and Engineering Physics,
830 Stevens Institute of Technology, Hoboken, NJ 07030, 2000.

831 Steinbrecht, W., Köhler, U., Claude, H., Weber, M., Burrows, J.P., and van der A, R.J.: Very high
832 ozone columns at northern mid-latitudes in 2010, Geophys Res Lett, 38, L06803,
833 doi:10.1029/2010GL046634, 2011.

834 Toledano, C., Cachorro, V.E., Berjon, A., de Frutos, A.M., Sorribas, M., de la Morena, B., and
835 Goloub, P.: Aerosol optical depth and Ångström exponent climatology at El Arenosillo
836 AERONET site (Huelva, Spain), Q. J. R. Meterol. Soc., 133, 795-807, 2007a.

837 Toledano, C., Cachorro, V.E., de Frutos, A.M., Sorribas, M., Prats, N., and de la Morena, B.:
838 Inventory of African desert dust events over the southwestern Iberian Peninsula in 2000-2005
839 with an AERONET Cimel Sun photometer, J. Geophys. Res. 112, doi:10.1029/2006JD008307,
840 2007b.

841 Valenzuela, A., Olmo, F.J., Lyamani, H., Antón, M., Quirantes, A., and Alados-Arboledas, L.:
842 Aerosol radiative forcing during African desert dust events (2005-2010) over Southeastern
843 Spain, Atmos. Chem. Phys. 12, 10331–10351, doi:10.5194/acp-12-10331-2012, 2012.

844 Zhou, M., Yu, H., Dickinson, R. E., Dubovik, O., and Holben, B. N.: A normalized description of
845 the direct effect of key aerosol types on solar radiation as estimated from Aerosol Robotic
846 Network aerosols and Moderate Resolution Imaging Spectroradiometer albedos, J. Geophys.
847 Res., 110, D19202, doi:10.1029/2005JD005909, 2005.

848

Tables

Table 1. Coordinates and time interval of the six AERONET sites used in this study.

Station	Latitude (ºN)	Longitude (ºE)	Altitude a.s.l. (m)	Time interval
Palencia	41.99	-4.52	750	2003-2012
Barcelona	41.39	2.12	125	2004-2012
Cabo da Roca	38.78	-9.50	140	2003-2011
Évora	38.57	-7.91	293	2005-2012
Granada	37.16	-3.61	680	2004-2012
El Arenosillo	37.11	-6.73	0	2000-2009

Table 2. Summary of AERONET data used for ARE calculations: aerosol optical depth (AOD), single scattering albedo (SSA), asymmetry factor (g), precipitable water vapor column (PWC). Estimated absolute uncertainty of AOD and SSA is given according to Dubovik et al. (2002), and PWC error from Holben et al. (1998).

	AERONET database	Estimated uncertainty
AOD	Level 2.0	±0.01-0.02
SSA, g (AOD_{440}>0.4)	Level 2.0	±0.03 (in SSA)
SSA, g (0.15<AOD_{440}<0.4)	Level 1.5-filtered*	±0.05-0.07(in SSA)
SSA, g (AOD_{440}<0.15)	Fixed value	
PWC	Level 2.0	10-15%

*Filters applied are the same as in level 2.0 except for AOD_{440} (see text).

Table 3. AFE values and their standard error for the UV, VIS, NIR, and SW ranges for, separately, four SSA and three α intervals over the Iberian Peninsula. Units are $Wm^{-2}\tau^{-1}$. SSA groups: $0.85 \geq SSA_1 > 0.80$ (group 1), $0.90 \geq SSA_2 > 0.85$ (group 2), $0.95 \geq SSA_3 > 0.90$ (group 3), and $1.0 \geq SSA_4 > 0.95$ (group 4); and α groups: $0 \leq \alpha_1 \leq 1$ (group 1), $1.0 \leq \alpha_2 \leq 1.5$ (group 2), and $1.5 < \alpha_3 \leq 2$ (group 3). The average values without any classification are also presented.

Variable	Group	AFE_{UV}	AFE_{VIS}	AFE_{NIR}	AFE_{SW}
α	1	-5.41 ± 0.06	-30.1 ± 0.3	-20.9 ± 0.2	-56.5 ± 0.5
	2	-6.60 ± 0.09	-38.3 ± 0.4	-19.1 ± 0.2	-64.0 ± 0.6
	3	-7.06 ± 0.10	-39.4 ± 0.4	-16.9 ± 0.2	-63.3 ± 0.7
SSA	1	-9.7 ± 0.2	-52.8 ± 0.8	-24.9 ± 0.5	-87.4 ± 1.4
	2	-8.19 ± 0.10	-44.6 ± 0.4	-21.2 ± 0.2	-74.0 ± 0.6
	3	-6.37 ± 0.05	-35.9 ± 0.2	-19.5 ± 0.2	-61.8 ± 0.3
	4	-4.59 ± 0.05	-26.6 ± 0.2	-18.1 ± 0.2	-49.3 ± 0.3
Average		-5.98 ± 0.05	-33.7 ± 0.2	-19.34 ± 0.11	-59.1 ± 0.3

Table 4. Daily Forcing Efficiencies at the surface by previous studies. Legend: desert dust (DD), continental-biomass burning (C-BB), and forest fires (FF).

Reference	Aerosol Type	AFE_X	Value ($Wm^{-2}\tau^{-1}$)	Time period	Region	More info.
Díaz et al. (2007)	Mixed	AFE_{UV}	-3	July 2002	Spain	290-363 nm
Meloni et al. (2005)	DD Mixed	AFE_{VIS}	-28.4 -45.6	July 2002	Central Mediterranean	
Lyamani et al. (2006)	Mixed	AFE_{VIS}	-75.8	August 2003	Spain	2003 heat wave
Di Biagio et al. (2010)	DD C-BB Mixed	AFE_{SW}	-68.9 -59.0 -94.9	2004-2007	Central Mediterranean	At the equinox
Esteve et al. (2014)	Mixed	AFE_{SW}	-139.0	2003-2011	Spain	200 cloud-free days
Santos et al. (2008)	FF	AFE_{SW}	-113.0	2004-2005	Portugal	Absorbing aerosols
di Sarra et al. (2011)	DD	AFE_{SW}	-55	25-26/03/2010	Central Mediterranean	Strong event
García et al. (2014)	DD	AFE_{SW}	-59	2009-2012	Canary Islands	386 cloud-free days
Costa et al. (2006)	DD	AFE_{SW}	-116.9	7/04/2000	Korea	SSA = 0.76
Zhou et al. (2005)	DD	AFE_{SW}	-80/-48	Monthly aerosol climatology	North Africa and Arabian Peninsula	Depending on surface albedo
Saha et al. (2008)	C-BB Mixed	AFE_{SW}	-97.6 -81.5	2005-2006	French Mediterranean	0.7 < SSA < 0.8
Valenzuela et al. (2012)	DD	AFE_{SW}	-70	2005-2010	Spain	

Table A1. Mean relative difference (RD) in the UV, VIS, NIR, and SW net fluxes if SSA = 0.90 and g = 0.75 are compared with different SSA and g scenarios for different SZA values.

SZA	RD_{UV} (%)	RD_{VIS} (%)	RD_{NIR} (%)	RD_{SW} (%)
30	±3.4	±1.9	±0.9	±1.5
60	±4.9	±3.0	±1.5	±2.4

885 Figure Captions

886 **Figure 1.** Annual cycle of daily values of AOD at 440 nm by box whisker plots. Triangles and
887 horizontal solid lines indicate the monthly average and median values, respectively.

888 **Figure 2.** Annual cycle of daily values of α ('alpha' in the figure) by box whisker plots. Triangles
889 and horizontal solid lines indicate the monthly average and median values, respectively.

890 **Figure 3.** Relative frequency of aerosol type occurrence: maritime (MA), desert dust (DD),
891 continental clean (CC), and continental polluted (CP).

892 **Figure 4.** Yearly values of AOD_{440nm} at the six sites: Barcelona (blue diamonds), Palencia (purple
893 triangles), Évora (red squares), Cabo da Roca (grey crosses), Granada (black stars), and El
894 Arenosillo (green circles). The text points out the statistically significant trend obtained.

895 **Figure 5.** Evolution of yearly ARE_{UV} (a), ARE_{VIS} (b), ARE_{NIR} (c), and ARE_{SW} (d) at the six sites:
896 Barcelona (blue diamonds), Palencia (purple triangles), Évora (red squares), Cabo da Roca (grey
897 crosses), Granada (black stars), and El Arenosillo (green circles). Vertical bars indicate the standard
898 deviation of each yearly value at Palencia station.

899 **Figure 6.** Evolution of annual ARE at the four spectral ranges (ARE_{UV} purple diamonds, ARE_{VIS}
900 red squares, ARE_{NIR} green triangles, and ARE_{SW} black circles) and AOD at 500 nm (blue stars)
901 averaging the data from the six Iberian ground-based sites (only years with at least three sites
902 considered). Dashed lines point out the linear trends (see text).

903 **Figure 7.** Annual cycle of ARE_{UV} (a), ARE_{VIS} (b), ARE_{NIR} (c), and ARE_{SW} (d) at the six sites:
904 Barcelona (blue diamonds), Palencia (purple triangles), Évora (red squares), Cabo da Roca (grey
905 crosses), Granada (black stars), and El Arenosillo (green circles). Vertical bars point out the
906 standard deviation of each monthly value at Évora station.

907 **Figure 8.** AFE_{UV}, AFE_{VIS}, AFE_{NIR}, and AFE_{SW} against four groups of aerosol single scattering
908 albedo and three intervals of α at the six sites: Barcelona (blue diamonds), Palencia (purple
909 triangles), Évora (red squares), Cabo da Roca (grey crosses), Granada (black stars), and El
910 Arenosillo (green circles).

911 **Figure 9.** Dependence of AFE_{VIS}/AFE_{SW} (a, c, e) and AFE_{NIR}/AFE_{SW} (b, d, f) ratios on SSA for
912 large (a, b), medium (c, d) and small (e, f) particles at the six sites: Barcelona (blue diamonds),
913 Palencia (purple triangles), Évora (red squares), Cabo da Roca (grey crosses), Granada (black stars),
914 and El Arenosillo (green circles).

915

916 Figure 1

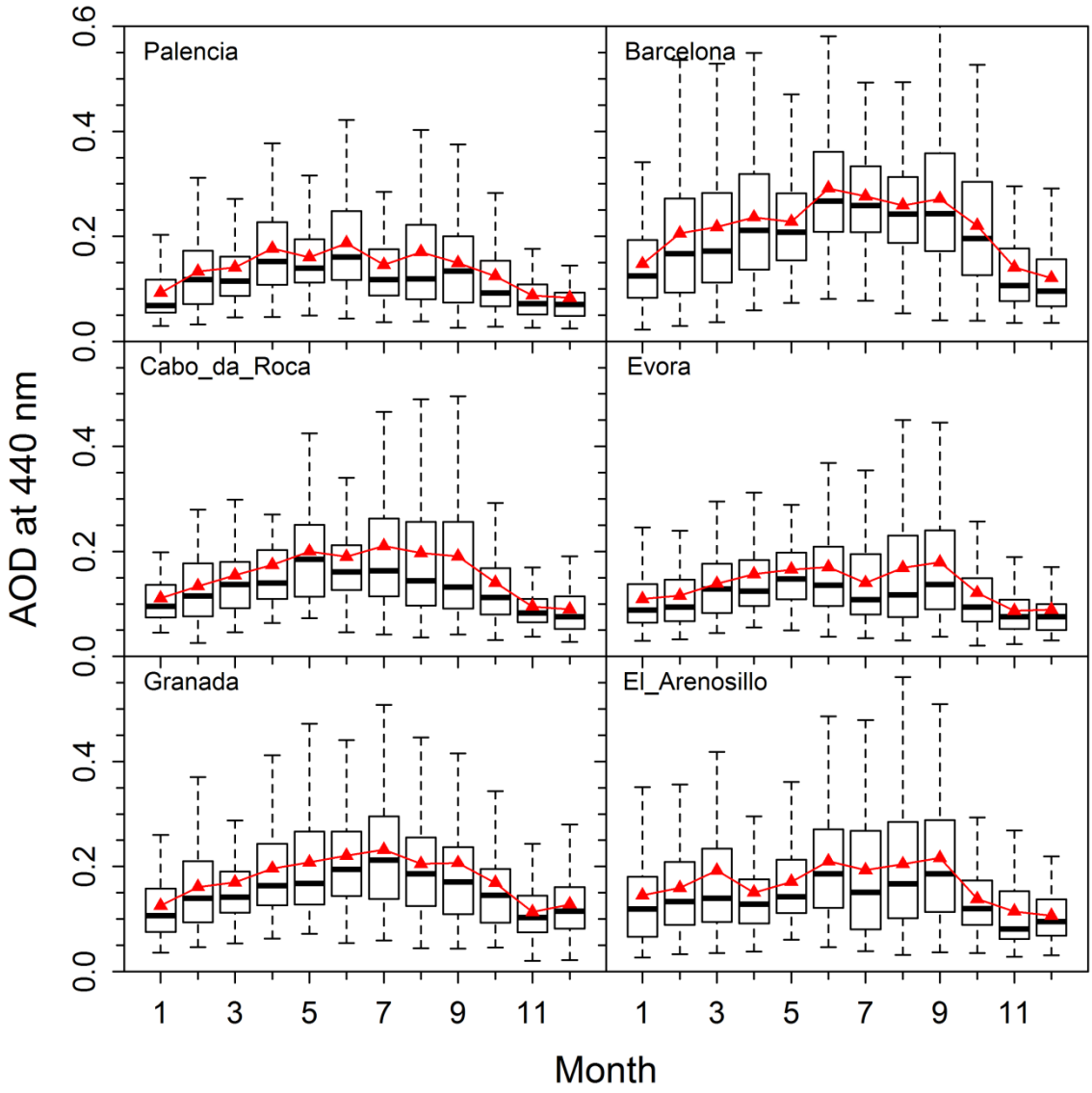

917

918 **Figure 1.** Annual cycle of daily values of AOD at 440 nm by box whisker plots. Triangles and

919 horizontal solid lines indicate the monthly average and median values, respectively.

920

921 Figure 2

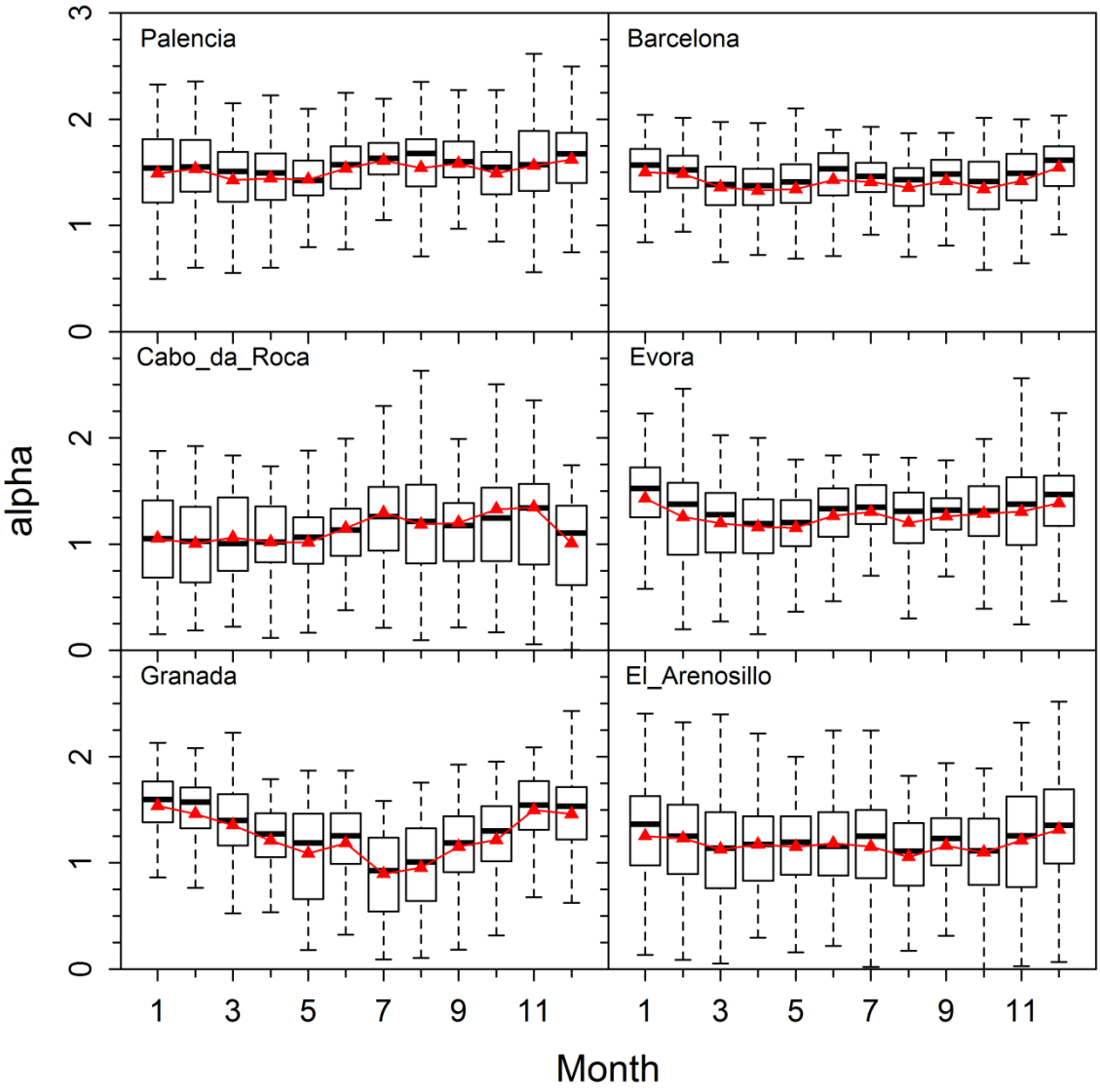

922

923 **Figure 2.** Annual cycle of daily values of α ('alpha' in the figure) by box whisker plots. Triangles
924 and horizontal solid lines indicate the monthly average and median values, respectively.

925

926

927 Figure 3

928

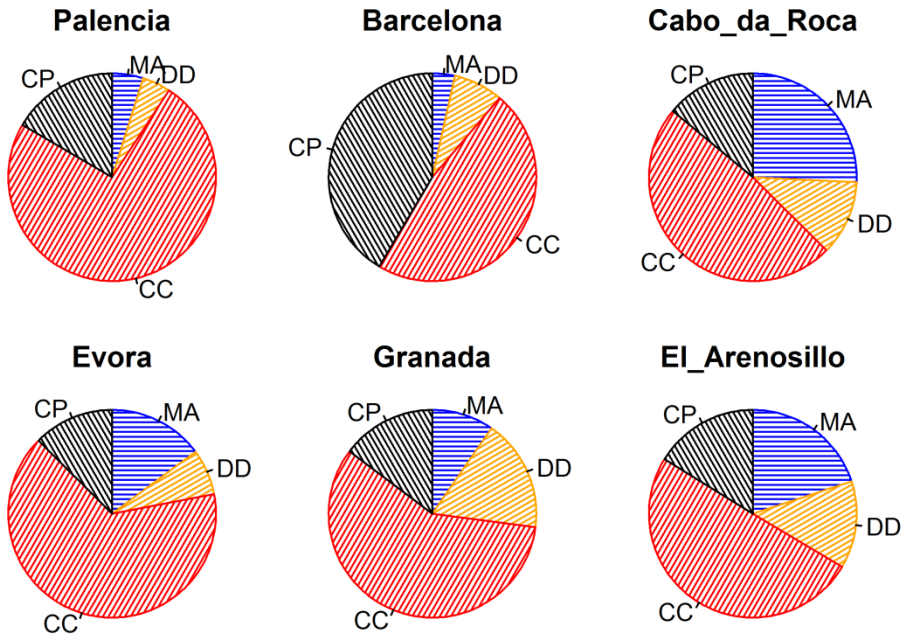

929

930 **Figure 3.** Relative frequency of aerosol type occurrence: maritime (MA), desert dust (DD),
931 continental clean (CC), and continental polluted (CP).

932

933 Figure 4

934

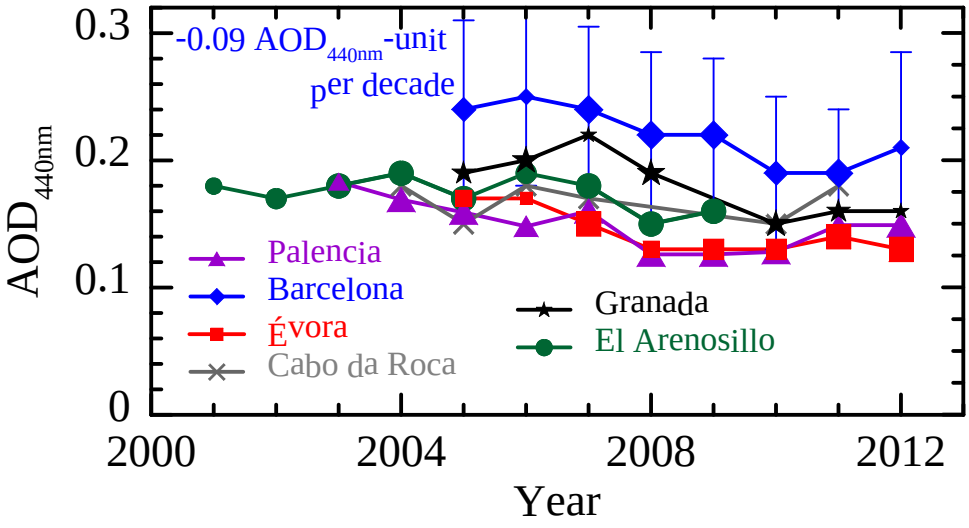

935

936 **Figure 4.** Yearly values of AOD_{440nm} at the six sites: Barcelona (blue diamonds), Palencia (purple
937 triangles), Évora (red squares), Cabo da Roca (grey crosses), Granada (black stars), and El
938 Arenosillo (green circles). The text points out the statistically significant trend obtained. Vertical
939 bars indicate the standard deviation of each yearly value at Barcelona station. Larger the symbols,
940 large amount of data number that year.

941

942 Figure 5

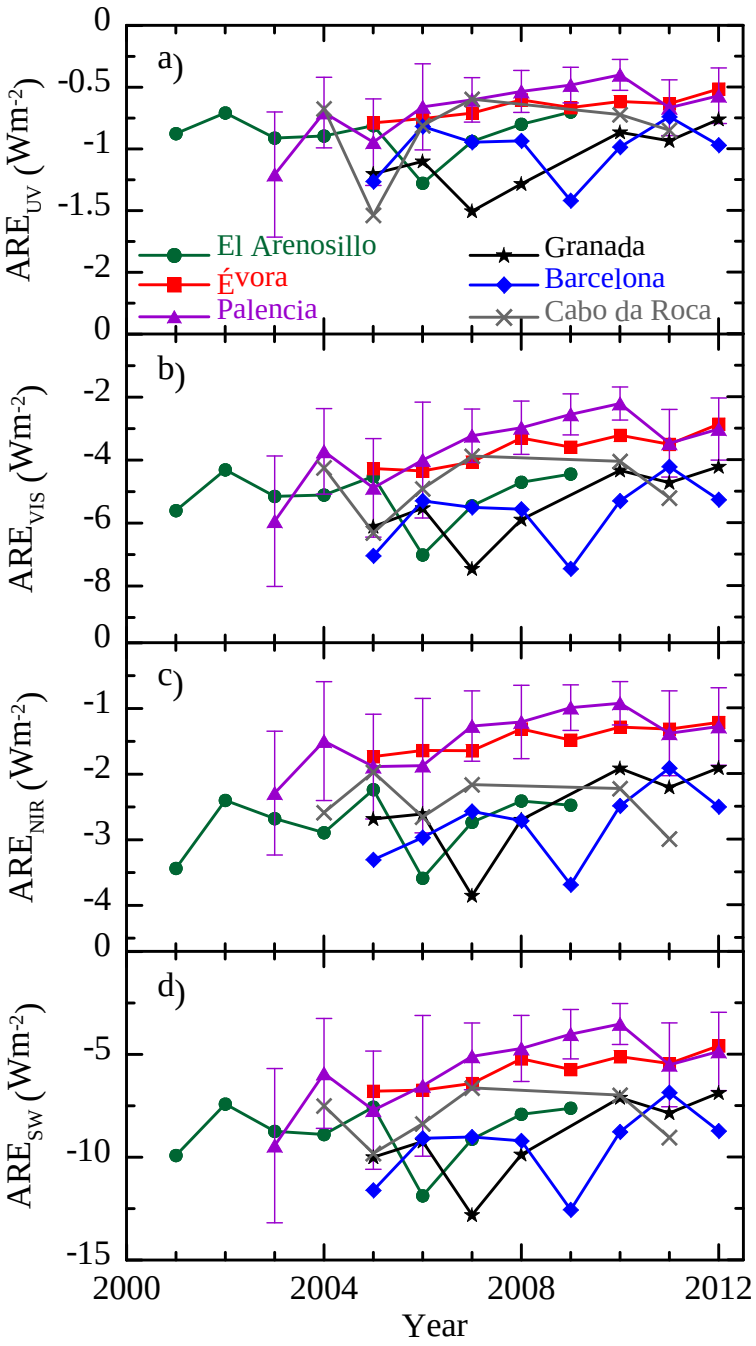

943

944 **Figure 5.** Evolution of yearly ARE$_{UV}$ (a), ARE$_{VIS}$ (b), ARE$_{NIR}$ (c), and ARE$_{SW}$ (d) at the six sites:
945 Barcelona (blue diamonds), Palencia (purple triangles), Évora (red squares), Cabo da Roca (grey
946 crosses), Granada (black stars), and El Arenosillo (green circles). Vertical bars indicate the standard
947 deviation of each yearly value at Palencia station.

948 Figure 6
949
950

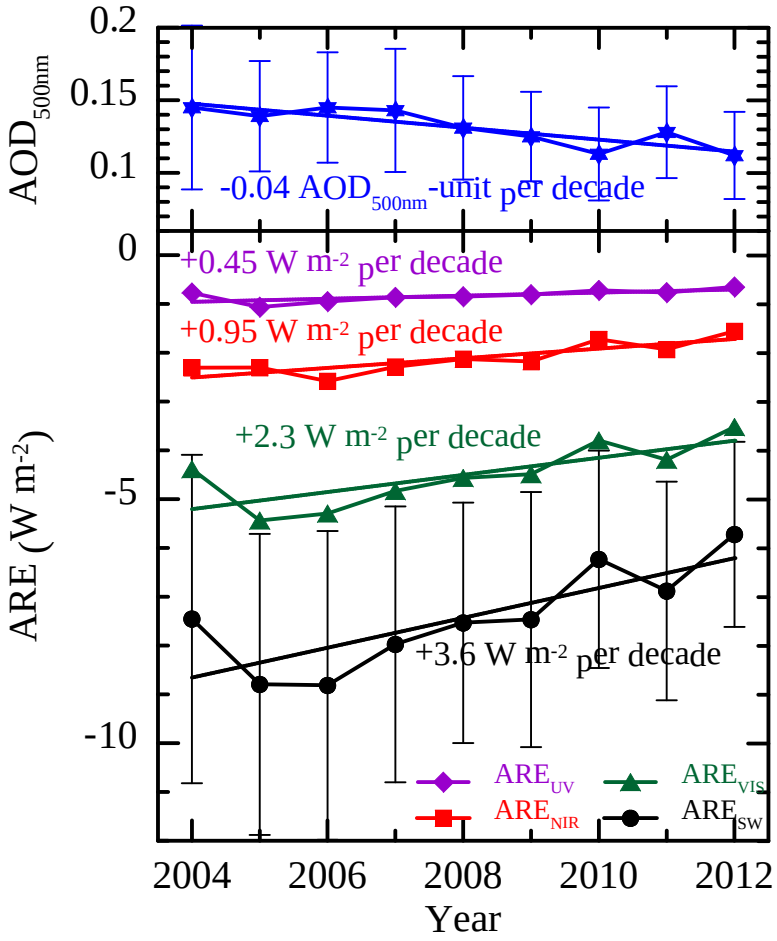

951
952

953 **Figure 6.** Evolution of annual ARE at the four spectral ranges (ARE_{UV} purple diamonds, ARE_{VIS}
954 red squares, ARE_{NIR} green triangles, and ARE_{SW} black circles) and AOD at 500 nm (blue stars)
955 averaging the data from the six Iberian ground-based sites (only years with, at least, three sites are
956 considered). Dashed lines point out the linear trends (see text). Vertical bars indicate the standard
957 deviation.

958

959 Figure 7
960

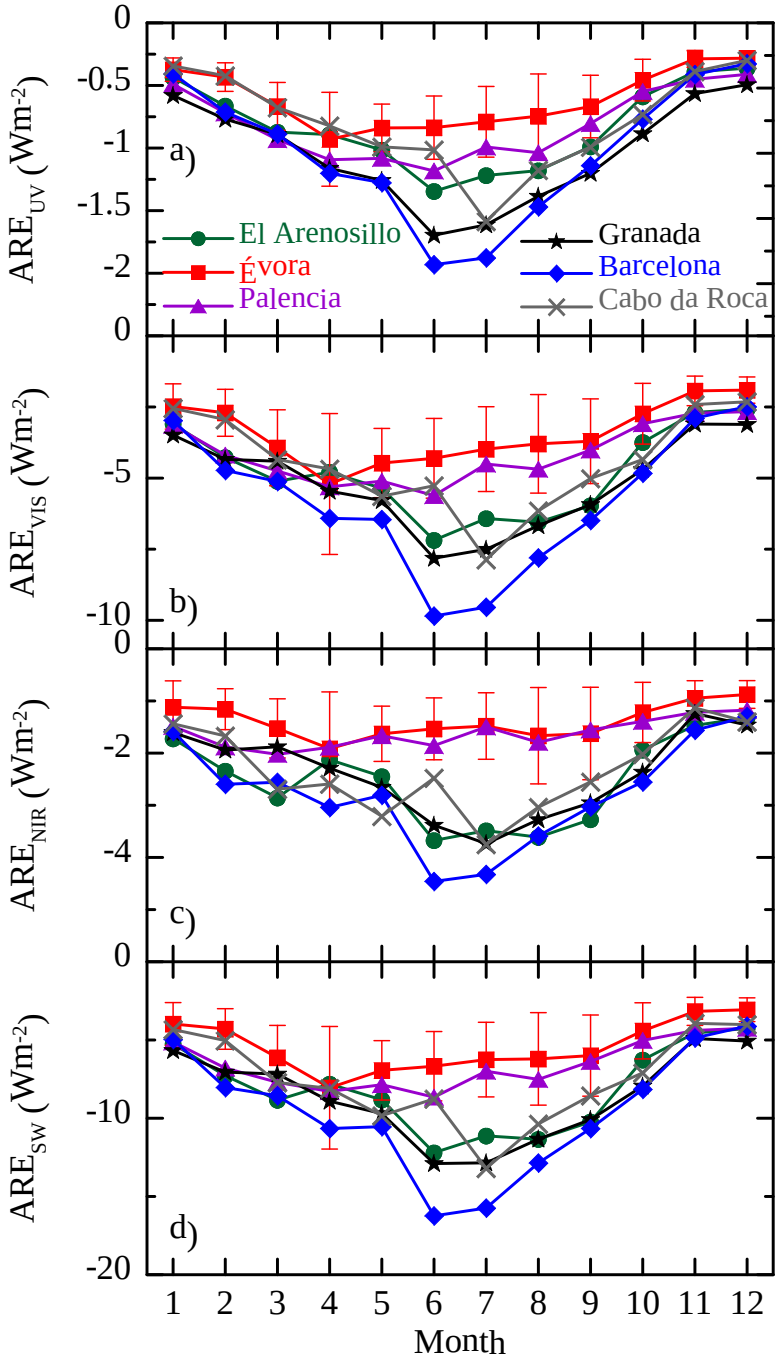

961

962 **Figure 7.** Annual cycle of ARE_{UV} (a), ARE_{VIS} (b), ARE_{NIR} (c), and ARE_{SW} (d) at the six sites:
963 Barcelona (blue diamonds), Palencia (purple triangles), Évora (red squares), Cabo da Roca (grey
964 crosses), Granada (black stars), and El Arenosillo (green circles). Vertical bars point out the
965 standard deviation of each monthly value at Évora station.

Figure 8

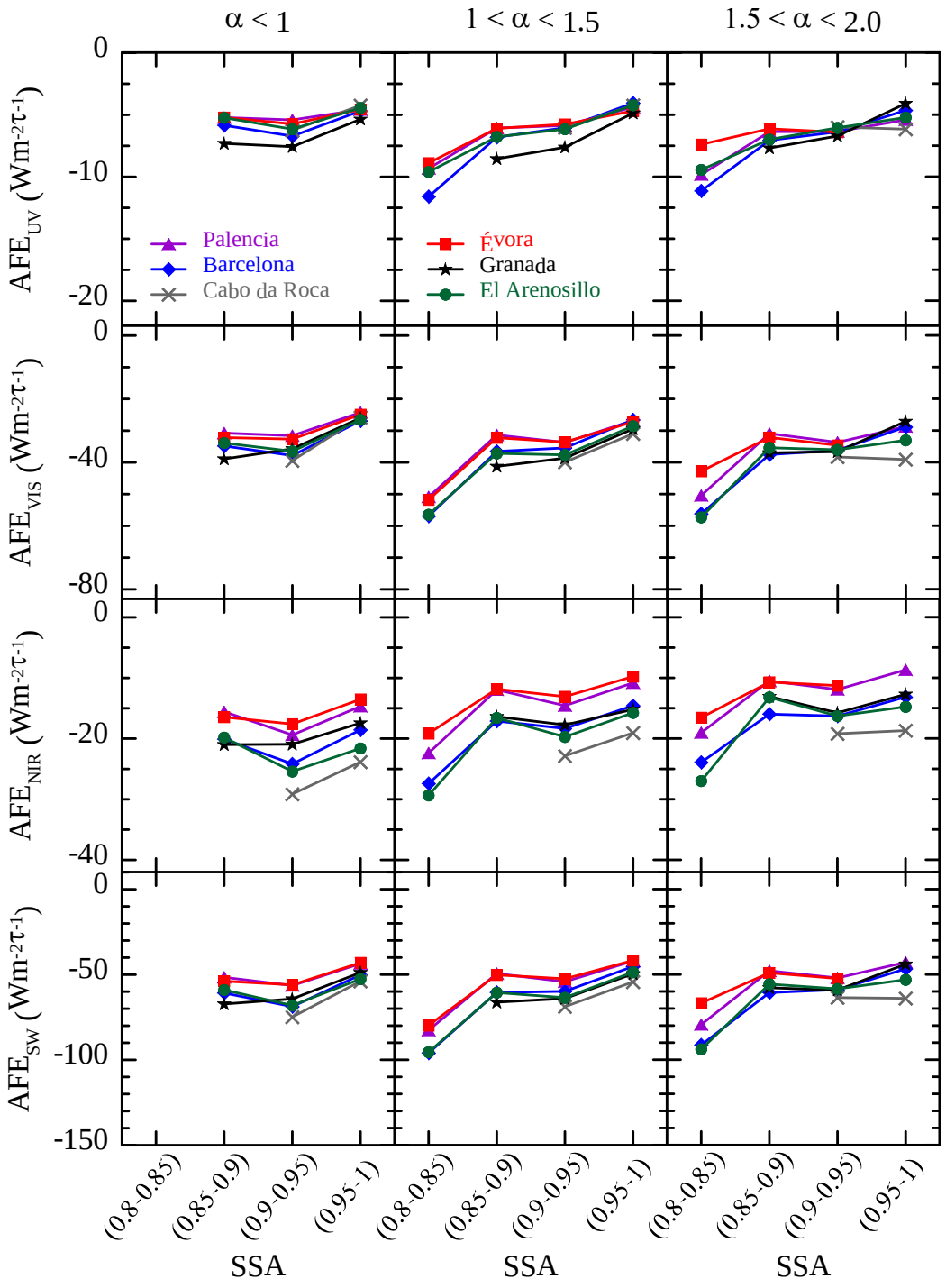

Figure 8. AFE_{UV}, AFE_{VIS}, AFE_{NIR}, and AFE_{SW} against four groups of aerosol single scattering albedo and three intervals of α at the six sites: Barcelona (blue diamonds), Palencia (purple triangles), Évora (red squares), Cabo da Roca (grey crosses), Granada (black stars), and El Arenosillo (green circles).

Figure 9

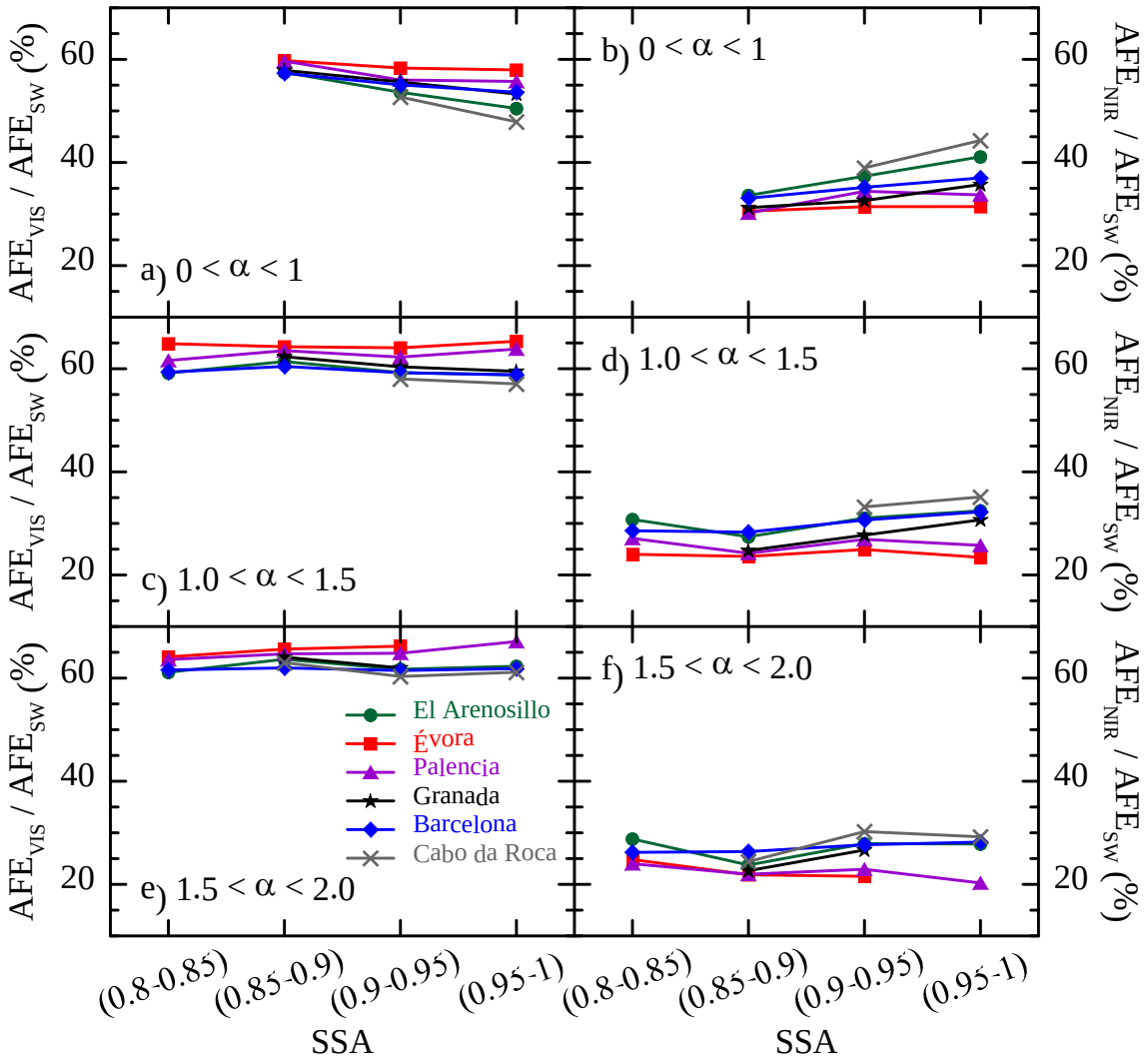

Figure 9. Dependence of AFE_{VIS}/AFE_{SW} (a, c, e) and AFE_{NIR}/AFE_{SW} (b, d, f) ratios on SSA for large (a, b), medium (c, d) and small (e, f) particles at the six sites: Barcelona (blue diamonds), Palencia (purple triangles), Évora (red squares), Cabo da Roca (grey crosses), Granada (black stars), and El Arenosillo (green circles).

980 Figure A1

981

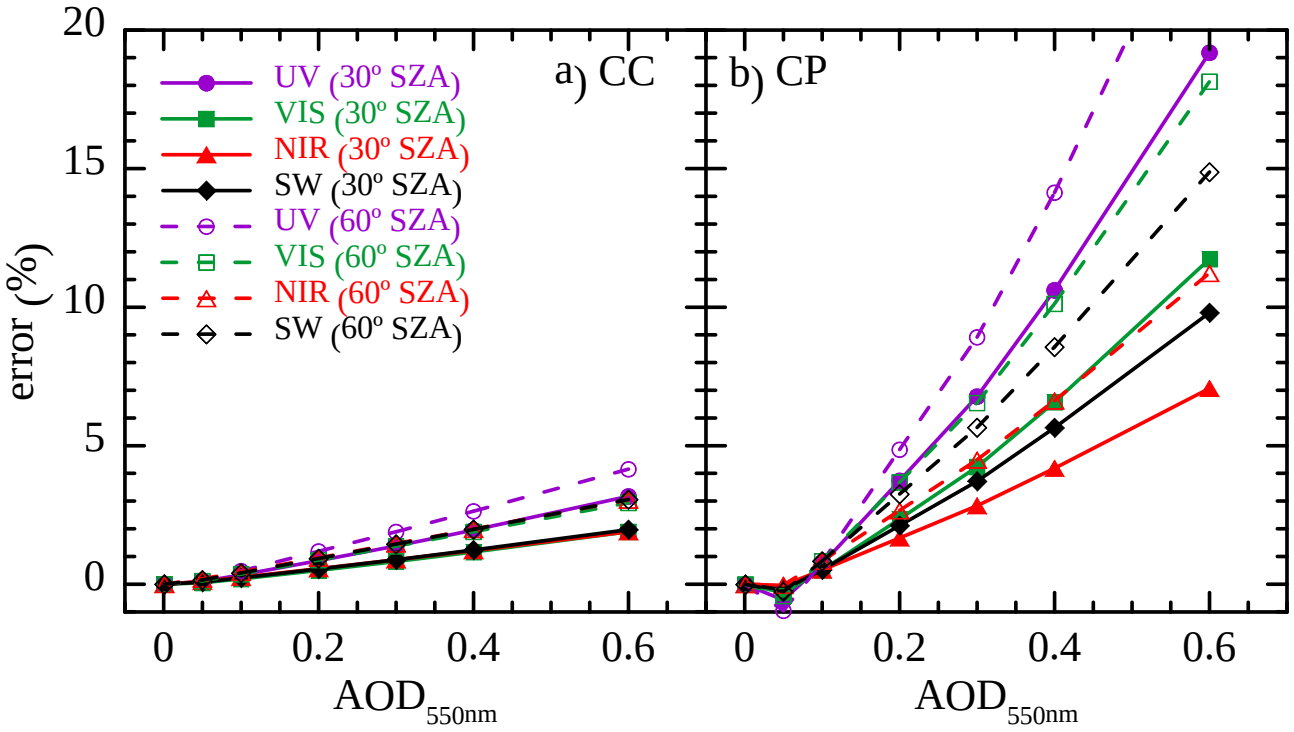

982

983 Figure A1. Evolution of the error committed when the optical properties are fixed in the different
984 spectral range for two SZAs, and continental clean (CC, a) and continental polluted (CP, b)
985 aerosols.

986